frontiers in Materials

REVIEW
published: 24 February 2022
doi: 10.3389/fmats.2022.812984

Recent Progress in Crystallographic Characterization, Magnetoresponsive and Elastocaloric Effects of Ni-Mn-In-Based Heusler Alloys—A Review

Hai-Le Yan[1]*, *Xiao-Ming Huang*[1] and *Claude Esling*[2]*

[1]Key Laboratory for Anisotropy and Texture of Materials (Ministry of Education), School of Material Science and Engineering, Northeastern University, Shenyang, China, [2]Laboratoire d'Étude des Microstructures et de Mécanique des Matériaux (LEM3), CNRS UMR 7239, Université de Lorraine, Metz, France

Ni-Mn-In-based magnetic shape memory alloys have promising applications in numerous state-of-the-art technologies, such as solid-state refrigeration and smart sensing, resulting from the magnetic field-induced inverse martensitic transformation. This paper aims at presenting a comprehensive review of the recent research progress of Ni-Mn-In-based alloys. First, the crystallographic characterization of these compounds that strongly affects functional behaviors, including the crystal structure of modulated martensite, the self-organization of martensite variants and the strain path during martensitic transformation, are reviewed. Second, the current research progress in functional behaviors, including magnetic shape memory, magnetocaloric and elastocaloric effects, are summarized. Finally, the main bottlenecks hindering the technical development and some possible solutions to overcome these difficulties are discussed. This review is expected to provide some useful insights for the design of novel advanced magnetic shape memory alloys.

Keywords: NiMnIn, modulated martensite, martensitic transformation, magnetocaloric effect, elastocaloric effect

OPEN ACCESS

Edited by:
Vincent G. Harris,
Northeastern University, United States

Reviewed by:
Durga Paudyal,
Iowa State University, United States
Francesca Casoli,
Italian National Research Council, Italy

***Correspondence:**
Hai-Le Yan
yanhaile@mail.neu.edu.cn
Claude Esling
claude.esling@univ-lorraine.fr

Specialty section:
This article was submitted to Smart Materials, a section of the journal Frontiers in Materials

Received: *11 November 2021*
Accepted: *31 January 2022*
Published: *24 February 2022*

Citation:
Yan H-L, Huang X-M and Esling C (2022) Recent Progress in Crystallographic Characterization, Magnetoresponsive and Elastocaloric Effects of Ni-Mn-In-Based Heusler Alloys—A Review. Front. Mater. 9:812984. doi: 10.3389/fmats.2022.812984

1 INTRODUCTION

In 1996, a large magnetic-field-induced strain, i.e., 0.2% under a magnetic field of 0.8 T realized by the rearrangement of martensite variants driven by the magnetocrystalline anisotropy energy, was first reported in the stoichiometric Heusler-type Ni_2MnGa alloys by K. Ullakko and collaborators (Ullakko et al., 1996). Compared with the magnetostrictive materials, such as Terfenol-D, and conventional shape memory alloys, such as Ni-Ti, the magnetic-field-induced strain in Ni_2MnGa has both fast responsive frequency and large output strain, and thus is considered to have huge potential in the fields of smart actuators and sensors. From then on, the Heusler-type NiMnGa alloy has aroused widespread attention (Zheludev et al., 1996; Mañosa et al., 1997; Planes et al., 1997; Ullakko et al., 1997; Brown et al., 1999). About 10 years later, Y. Sutou and R. Kainuma et al. fabricated a series of nonstoichiometric Ni(Co)MnZ (Z = In, Sn and Sb) Heusler-type alloys by the replacement of the *p-block* type Ga by Z (Z = In, Sn or Sb) (Sutou et al., 2004a). Although Ga ($4s^2p^1$) and In ($5s^2p^1$) belong to the same main-group elements (IIIA) and their positions in the elemental periodic table are adjacent, the magnetic properties and the resultant functional behaviors of NiMnGa and NiMnIn are significantly different.

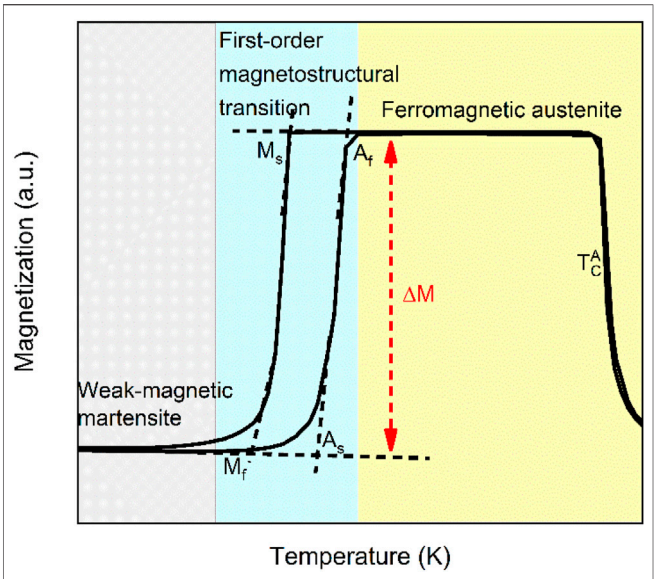

FIGURE 1 | Typical temperature dependence of magnetization (M-T curve) for the NiMnIn-based alloys.

Specifically, the magnetization of martensite and austenite are similar in NiMnGa, while the magnetization of martensite in the NiMnIn is much weaker than that of austenite, as shown in **Figure 1**. In other words, for the NiMnIn-based alloys, there is a significant change in magnetism during the martensitic transformation, and thus this transition is also termed the magnetostructural transition. As a result, the Zeeman energy ($E_{Zeeman} = -\mu_0 \int MHdV$) of austenite, i.e., the potential energy of a magnetized body having magnetization M and a volume of V in an external magnetic field H, should be much lower than that of martensite. Thus, the magnetic field should stabilize the strong magnetic austenite phase. This feature of the NiMnIn alloy provides an extra stimulus, apart from thermal and mechanical fields, to drive the inverse martensitic transformation. To be specific, when a magnetic field is applied to the martensite of the NiMnIn alloy, the sample tends to transform to the austenite state, i.e., the magnetic-field-induced inverse martensite transformation, under the driving force of the Zeeman energy difference $\mu_0 H\Delta M$ of these two phases.

If a pre-strain is applied to the martensite before the application of a magnetic field, during the magnetic-field-induced inverse martensite transformation, the sample tends to recover its original shape, which is termed as the metamagnetic shape-memory effect (Kainuma et al., 2006). Different from NiMnGa, in which the output stress (a few MPa) is limited by the magnetocrystalline anisotropy energy, the output stress of Ni(Co)MnIn can reach a large value (~100 MPa) since the Zeeman energy continues to increase with the elevated magnetic field (Karaca et al., 2006; Karaca et al., 2009). In addition, since the total entropy and the electric resistance of austenite and martensite have great differences, when an external magnetic field is applied, a huge change of total entropy (termed as the magnetocaloric effect) and electric resistance (termed as the magnetoresistance effect) may occur during the magnetic-field-induced inverse martensite transformation. Thus, the Ni(Co)MnIn alloys possess excellent magnetoresponsive performances (Han et al., 2006; Han et al., 2008; Kustov et al., 2009; Liu et al., 2012; Kihara et al., 2014), including magnetocaloric, magnetoresistance, and exchange bias effects. Besides, like the conventional shape memory alloy in which the martensitic transformation can be driven by thermal and mechanical fields, the Ni(Co)MnIn alloys also exhibit the thermal-induced shape memory, superelasticity, and elastocaloric effects (Mañosa et al., 2010; Lu et al., 2014; Moya et al., 2014; Liu et al., 2017; Manosa and Planes, 2017; Kabirifar et al., 2019).

During the past 15 years, scientists from all over the world have conducted continuous and in-depth research on NiMnIn-based alloys (Kainuma et al., 2008; Hu et al., 2013; Bachaga et al., 2019). Numerous systematic and in-depth research results covering crystal structure, morphological and crystallographic features of microstructure, martensitic transformation, multifunctional behaviors, etc., have been reported in the literature. Therefore, a systematical overview of the current findings is of great significance to the development of this compound. To date, the metamagnetic shape memory, magnetocaloric, and elastocaloric effects of NiMnIn alloy have been briefly summarized and compared with other competitors in different review papers, such as the review paper about magnetic shape memory alloy by Kainuma et al. (2008), the paper focused on caloric materials by Moya et al. (2014), the review about mechanocaloric effect by Manosa and Planes (2017) and the paper focused on magnetic elastocaloric materials by Liu et al. (2017), and the review about magnetic refrigeration materials by Gottschall et al. (2019). Nevertheless, to the best of the authors' knowledge, there is still a lack of review articles focusing on the NiMnIn-based alloy in the literature.

This paper aims at presenting a comprehensive review of the research progress of Ni-Mn-In-based alloys. First, the crystallographic characterizations, including the crystal structure of austenite and modulated martensite (**Section 2**), the self-organization microstructure of modulated martensite (**Section 3**), and the transformation strain path of martensitic transformation (**Section 4**), are reviewed. Then, the current research progress in functional behaviors, including magnetic shape memory (**Section 5**), magnetocaloric (**Section 6**), and mechanocaloric (**Section 7**) effects, are summarized. For each topic, the main bottlenecks hindering the technical development and some possible solutions for overcoming these difficulties are discussed.

2 CRYSTAL STRUCTURE

The crystal structure is one of the most fundamental information of crystalline materials. In general, the determination of crystal structure is the first step to understanding the physical or mechanical properties of materials (Ravel et al., 2002b). Since the magnetostructural transition was discovered in the NiMnIn-based alloys, many state-of-the-art modern characterization

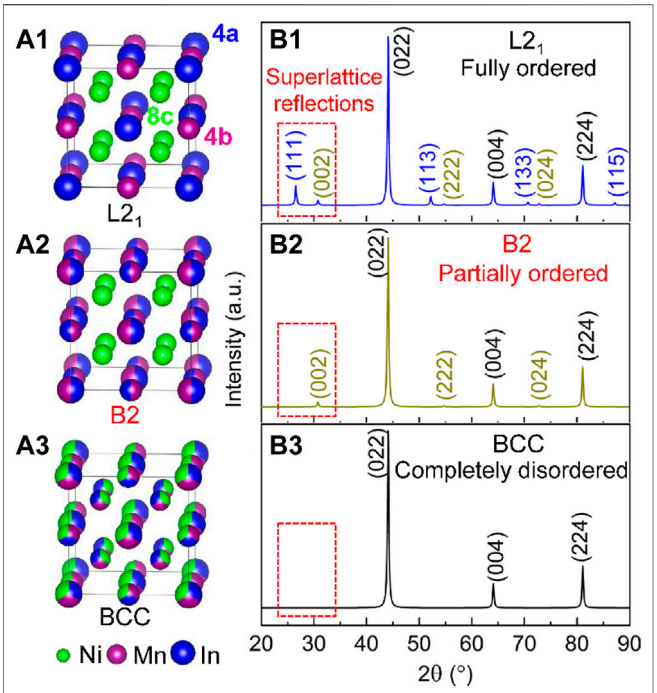

FIGURE 2 | Illustration of crystal structural models of $L2_1$ **(A_1)**, B2 **(A_2)**, and BCC **(A_3)** of NiMnIn alloy and their corresponding Cu Kα-radiation X-ray diffraction patterns **(B_1–B_3)**. To keep consistency with the $L2_1$ structure **(A_1)**, for the B2 **(A_2)** and the BCC **(A_3)** structures, the superstructural models containing 8 unit cells are illustrated. The main reflections in **(B_1–B_3)** are labeled with the black indices, while the superlattice reflections generated due to the B2 and the $L2_1$ types of stacking order of Ni, Mn, and In atoms are highlighted in olive and blue, respectively.

techniques, such as X-ray diffraction (XRD) (Liu et al., 2008; Feng et al., 2009; Zhang et al., 2014; Crouigneau et al., 2015; Paramanik and Das, 2016), synchrotron high-energy XRD (Karaca et al., 2009; Huang et al., 2016), neutron diffraction (Yan et al., 2015), high-resolution transmission electron microscope (HRTEM) (Yan et al., 2016c), selected area electron diffraction (SAED) (Ito et al., 2007; Ito et al., 2008; Liu et al., 2009a), high angle annular dark-field (HAADF) imaging of spherical aberration-corrected high-resolution scanning transmission electron microscope (Yang et al., 2020), have been used to characterize crystal structure of the compounds.

2.1 Austenite

2.1.1 Stoichiometric Ni_2MnIn

NiMnIn-based alloys belong to the Heusler-type alloys. The austenite phase of this compound has a typical structure of 2:1:1 full Heusler alloy, that is, a highly ordered cubic Cu_2MnAl-type $L2_1$ structure (space group: $Fm\bar{3}m$) (Heusler, 1934). **Figures $2A_1$,B_1** display the $L2_1$ structural model and a typical X-ray diffraction pattern, respectively. It is seen that the $L2_1$ structure is composed of four interpenetrated face-centered-cubic (FCC) sublattices, i.e., In: *4a* (0 0 0), Mn: *4b* (0.5 0.5 0.5), and Ni: *8c* (0.25 0.25 0.25) and (0.75 0.75 0.75). Theoretically, under 2θ ranging from 20° to 90°, there are three main reflections (labeled with the black indices), i.e., (022), (004) and (224), and seven satellite reflections (labeled with the blue and olive indices) due to the orderly stacking of Ni, Mn and In atoms, i.e., (111), (002), (113), (222), (133), (024) and (115), as shown in **Figure $2B_1$**.

As is known, the ordering degree of crystal structure significantly affects both mechanical and functional properties in the Heusler-type alloy (Ravel et al., 2002a; Raphael et al., 2002; Harris and Chen, 2015). For the NiMn-based alloys, the order degree of austenite is sensitive to the fabrication process and chemical composition (Krenke et al., 2006). When the alloy is quenched from a high temperature with a high cooling rate (such as melt-spinning technique), the austenite of NiMnIn alloy could exhibit the B2 type structure, as illustrated in **Figure $2A_2$**. The difference between the $L2_1$ and the B2 structures is that In and Mn atoms are orderly located at *4a* and *4b* sites in the former, whereas these two elements occupy the *4a* and *4b* sites randomly in the latter. Owing to the reduction of ordering degree, as shown in **Figure $2B_2$**, the number of satellite reflections decreases from 7 (the $L2_1$ structure) to 3 (the B2 structure), i.e., (002), (222), and (024). When the ordering degree further decreases, the B2 structure may turn to be the body-centered cubic (BCC) type. In this case, as shown in **Figure $2A_3$**, all Ni, Mn, and In atoms randomly occupy the *4a*, *4b,* and *8c* sites. For the XRD spectrum, the fully random occupations of Ni, Mn, and In atoms lead to the disappearance of all satellite diffraction peaks (**Figure $2B_3$**). Generally, the ordering degree of the austenite of the NiMnIn-based alloys can be evaluated by examining the number of satellite reflections at 2θ ranging from 25° to 35° (Cu Kα-radiation), as indicated in the red dashed boxes in **Figures $2A_1$–A_3**. Two (**Figure $2A_1$**), one (**Figure $2A_2$**), or zero (**Figure $2A_3$**) reflections suggest the austenite has the $L2_1$, the B2, or the BCC structure.

First-principles calculations showed that the exchange energy for In (*4a*) and Mn (*4b*) is around 70 meV/atom (Liu et al., 2020), which is smaller than that for Ni (*8c*) and Mn (*4b*) (around 85 meV/atom) (Liang et al., 2021). This result implies that the possibility of the occurrence of *4a*-*4b* disorder should be larger than that of *4a* (*4b*)-*8c* disorder, which explains the experimental results that the B2 structure is observed easier than the BCC structure. Moreover, from **Figures $2A_1$–A_3**, it is seen that even though the $L2_1$ structure is usually classified to be the face-centered cubic (FCC) structure from the point of view of crystallographic symmetry (Yan et al., 2016a; Lin et al., 2016), the atom stacking manner of the NiMnIn-based alloys mostly follows the characteristics of the BCC structure (with a different degree of ordering) rather than FCC. Thus, the typical structure characteristic parameters of the NiMnIn-based alloy, such as close-packed crystal plane, close-packed crystal direction, stacking density, coordination number, are the same as those of the BCC structure.

2.1.2 Non-stoichiometric NiMnIn Alloys

Unlike the NiMnGa alloys, where the stoichiometric case, i.e., Ni_2MnGa, undergoes a displacive structural transition at around 210 K (Wirth et al., 1997; Brown et al., 2002), the stoichiometric Ni_2MnIn is thermodynamically stable even when the temperature drops toward 0 K (Kurfiß et al., 2005; Krenke et al., 2006). Thus, the investigations on the NiMnIn-

based alloys are mostly focused on the nonstoichiometric compositions, especially the Mn-enriched Ni_2Mn(In, Mn) systems. Rietveld refinement of the high-resolution neutron diffraction data (Yan et al., 2015) showed that the extra-Mn prefers to directly substitute In at the 4a site. For the NiMnIn-based alloys, the magnetoresponsive behaviors are originated from the magnetic-field induced inverse martensitic transformation owing to the significant change of magnetization between austenite (ferromagnetism) and martensite (antiferromagnetism). Numerous studies suggested that the antiferromagnetism comes from the first-neighbored Mn (*4a*)-Mn(*4b*) coupling (Şaşıoğlu et al., 2004; Liu et al., 2006), which can be easily realized in the Mn-enriched Ni_2Mn(In, Mn) system since the extra-Mn tends to occupy the *4a* sites while the normal Mn is located at the *4b* sites (**Figure 2A$_2$**). This could be the reason why the fruitful magnetoresponsive behaviors of the NiMnIn-based alloys mostly exist in the Mn-enriched systems. By using the first-principles calculations, it is revealed that at the *4b* site, the extra-Mn atoms prefer to be dispersed from one another (Yan et al., 2015).

2.2 Martensite

For the martensite of the NiMnIn-based alloys, numerous studies showed that there exist two kinds of crystal structures, i.e., the non-modulated (NM) martensite and modulated martensite (Krenke et al., 2006). Note that even though the partial substitution of Co for Ni can significantly enhance the ferromagnetism of the NiMn-based alloys and thus improve their magnetoresponsive performances, this substitution will not change the type of crystal structure. Moreover, with the addition of Co, it is difficult to obtain a pure single-phase martensite powder sample, even if the testing temperature is far below the finishing temperature of martensitic transformation M_f measured by the DSC technique (Abematsu et al., 2014; Yan et al., 2015; Yan et al., 2016b). The reason could be attributed to the large specific surface area of the powder sample, which tends to stabilize the austenite and suppress the occurrence of martensitic transformation (Yan et al., 2021a). Thus, it is more convenient to determine the crystal structure of martensite with Co-free NiMnIn samples. X-ray diffraction studies showed that for the ternary Mn-enriched $Ni_{50}Mn_{50-x}In_x$ ($0 \le x \le 25$) alloys, the NM martensite structure exists in the alloys with a relatively low In content ($x \le 10$) (Yang et al., 2016). When $10 < x \le 16$, the martensite has a modulated structure. When the content of In continues to increase, the martensite transformation is arrested (Sutou et al., 2004b).

2.2.1 Non-modulated Martensite

For the $Ni_{50}Mn_{50-x}In_x$ alloys with a relatively low In content, it can be considered as In doped NiMn alloys. Actually, the crystal structure of the martensite of the $Ni_{50}Mn_{50-x}In_x$ ($x \le 10$) alloys is indeed the same as that of the stochiometric NiMn (Yang et al., 2016), i.e., the tetragonally distorted B2 structure. Nevertheless, to keep consistency with the $L2_1$ structure of austenite, as an equivalent structural model of the distorted B2 structure, the double $L1_0$ tetragonal cell proposed by J. Pons and coworkers

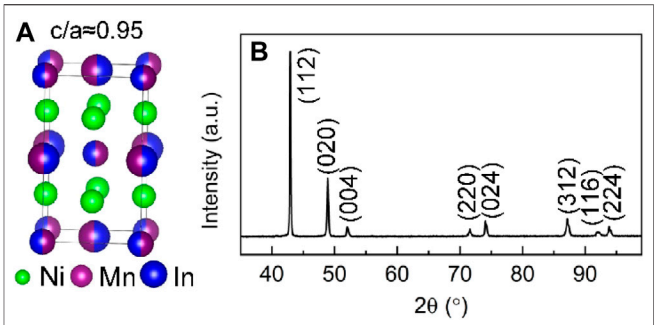

FIGURE 3 | Double $L1_0$ tetragonal structural model **(A)** and typical X-ray diffraction pattern **(B)** of the non-modulated martensite of the NiMnIn-based alloys.

(Pons et al., 2000) was extensively used in the literature to describe the non-modulated structure of martensite, as shown in **Figure 3A**. The space group of the double $L1_0$ tetragonal structure is I4/mmm (group number: 139). The atomic fractional coordinates of the different constituent elements in the NiMnIn alloys are as follows: Ni: *4d* (0, 0.5, 0.25); Mn and In: *2a* (0, 0, 0) and *2b* (0, 0, 0.5). The typical X-ray diffraction pattern of the non-modulated martensite is displayed in **Figure 3B**. Note that in this figure, the reflections are indexed based on the double $L1_0$ structural model rather than the distorted B2 model.

2.2.2 Modulated Martensite

With the increase of In content in the $Ni_{50}Mn_{50-x}In_x$ alloys, the crystal structure of martensite no longer follows the structure of NiMn (non-modulated double $L1_0$ tetragonal structure) and exhibits a long periodic layered modulated structure (Yang et al., 2016). For the NiMnIn-based alloys, the excellent magnetoresponsive performance mainly exists in the alloy systems with a modulated structure. Therefore, the accurate determination of the crystal structure for the modulated martensite is of significant importance for understanding and optimizing magnetoresponsive behaviors. Measured by neutron diffraction and synchrotron high-energy X-ray diffraction, and analyzed using the (3+1) dimensional superspace theory in combination with the Rietveld full-profile fitting method, the crystal structure of the modulated martensite of the NiMnIn alloys was determined with the $Ni_{50}Mn_{36}In_{14}$ alloy as a model material (Yan et al., 2015), as shown in **Figure 4A**. The basic idea of superspace theory is that by increasing the dimension of space, as shown in **Figure 4B**, the aperiodic structure can be mathematically transformed into a periodic one (Van Smaalen, 1995). Then, a unit cell can be defined in a higher-dimensional space and can thus be determined by fitting the diffraction data.

The determination process in Ref. (Yan et al., 2015) is as follows: 1) Construct the average crystal structure model of modulated martensite (ignoring atomic position modulation). Based on the crystal structure of austenite, combined with the splitting characteristics of neutron diffraction peaks during the martensitic transformation, the space group, the lattice constants, and the atom occupation information of the average crystal structure of the modulated martensite were determined.

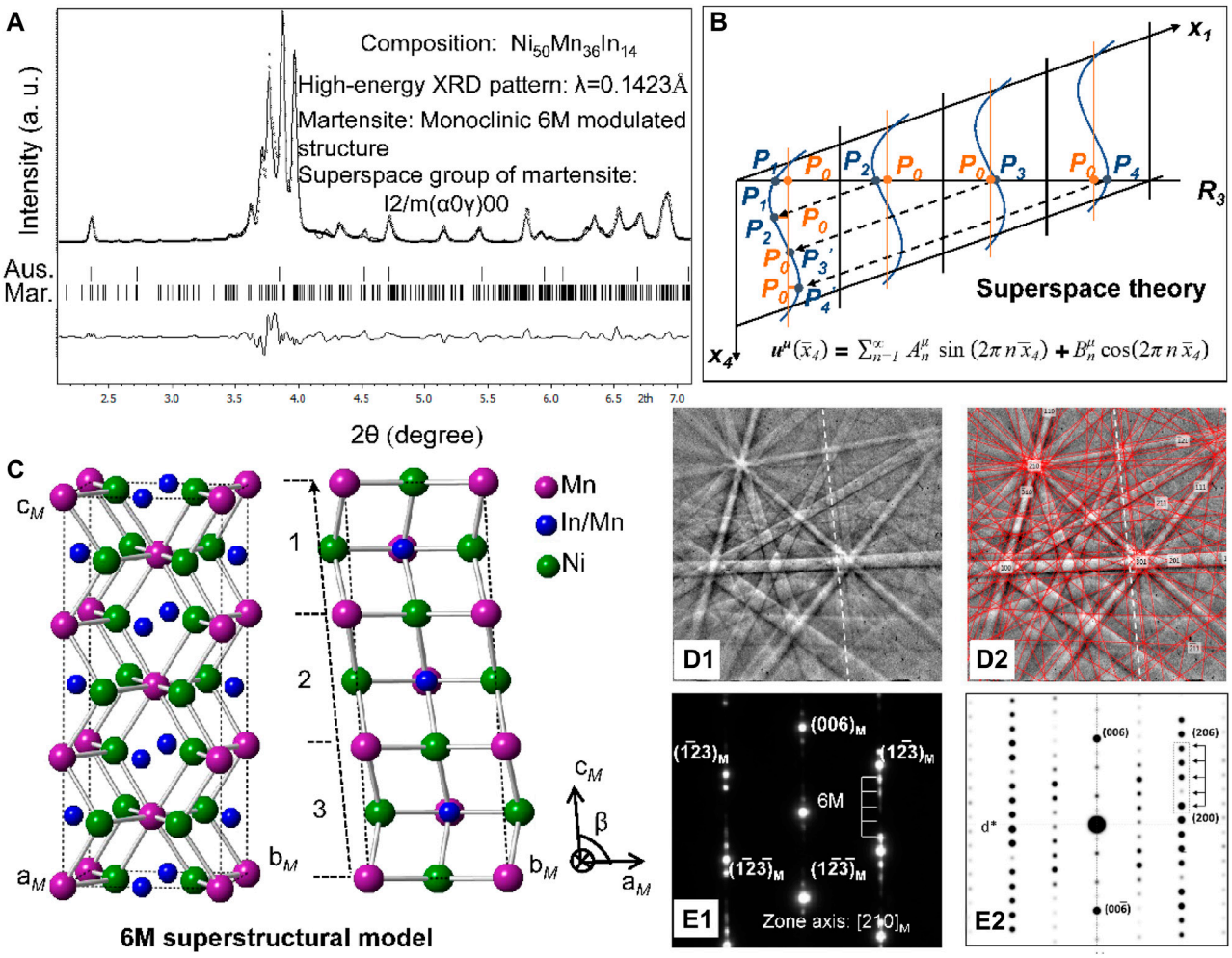

FIGURE 4 | (A) Rietveld full-profile refinement of high-energy synchrotron XRD pattern of the $Ni_{50}Mn_{36}In_{14}$ alloy by using the (3 + 1)-dimensional theory (Yan et al., 2015). **(B)** Basic idea of superspace theory, i.e., mathematically transforming the aperiodic structure to a periodic representation by increasing the dimension of space (x_4). **(C)** Established the three-dimensional 6M superstructural model with three consecutive averaging cells along the ***c*** axis. Measured **(D_1,E_1)** and simulated **(D_2,E_2)** SEM/EBSD Kikuchi and TEM selected area electron diffraction patterns (Yan et al., 2015). Reproduced with the permission of Elsevier Publisher.

2) Estimate the modulation wave vector ***q*** representing the modulation periodicity using the peak position of the satellite reflections caused by the periodic modulation of atom position. 3) Refine all structure information, including the coefficients of atom position modulation function, the lattice parameters, etc., with the high energy synchrotron X-ray diffraction pattern by means of the Rietveld method in the frame of the (3+1) dimensional superspace theory. 4) Analyze the rationality of the determined crystal structure information. 5) Build a three-dimensional superstructure model. A three-dimensional periodic superstructure model was established to approximately represent the determined modulated structure since many theoretical and experimental studies require the crystal structure information in the three-dimensional space.

Refinement showed that the modulated martensite has a monoclinic 6M modulated crystal structure and the space group is I2/m(α0γ)00, the lattice parameters of the average 1crystal structure are a = 4.3919 (4) Å, b = 5.6202 (1) Å, c = 4.3315 (7) Å, and β = 93.044 (1)°, and the modulation wave vector ***q*** = 0.343 (7) ***c**** (Yan et al., 2015). Since the coefficient of modulation wave vector ***q*** [0.343 (7)] is irrational, the structure should be incommensurate. The modulation wave vector can be described as ***q*** = 1/3(1+δ)***c**** , where δ (0.0312) represents the incommensurability. As δ is very small, the determined incommensurable 6M modulated structure can be approximately described using a superstructural model containing three average crystal structure cells along the ***c*** axis, as shown in **Figure 4C**. The space group of the established superstructural model is P2/m, and the lattice constants are a = 4.3919 (4) Å, b = 5.6202 (1) Å, c = 12.9947 (1) Å and β = 93.044 (1)°. For the detailed atomic occupation information, the readers can refer to Ref. (Yan et al., 2015). It is seen from **Figure 4C** that the shuffling character of the atomic layers is the same as that of the $(2\bar{1})_2$ Zhdanov sequence. To verify the accuracy of the established superstructure model, the EBSD Kikuchi pattern and the TEM selected area electron diffraction

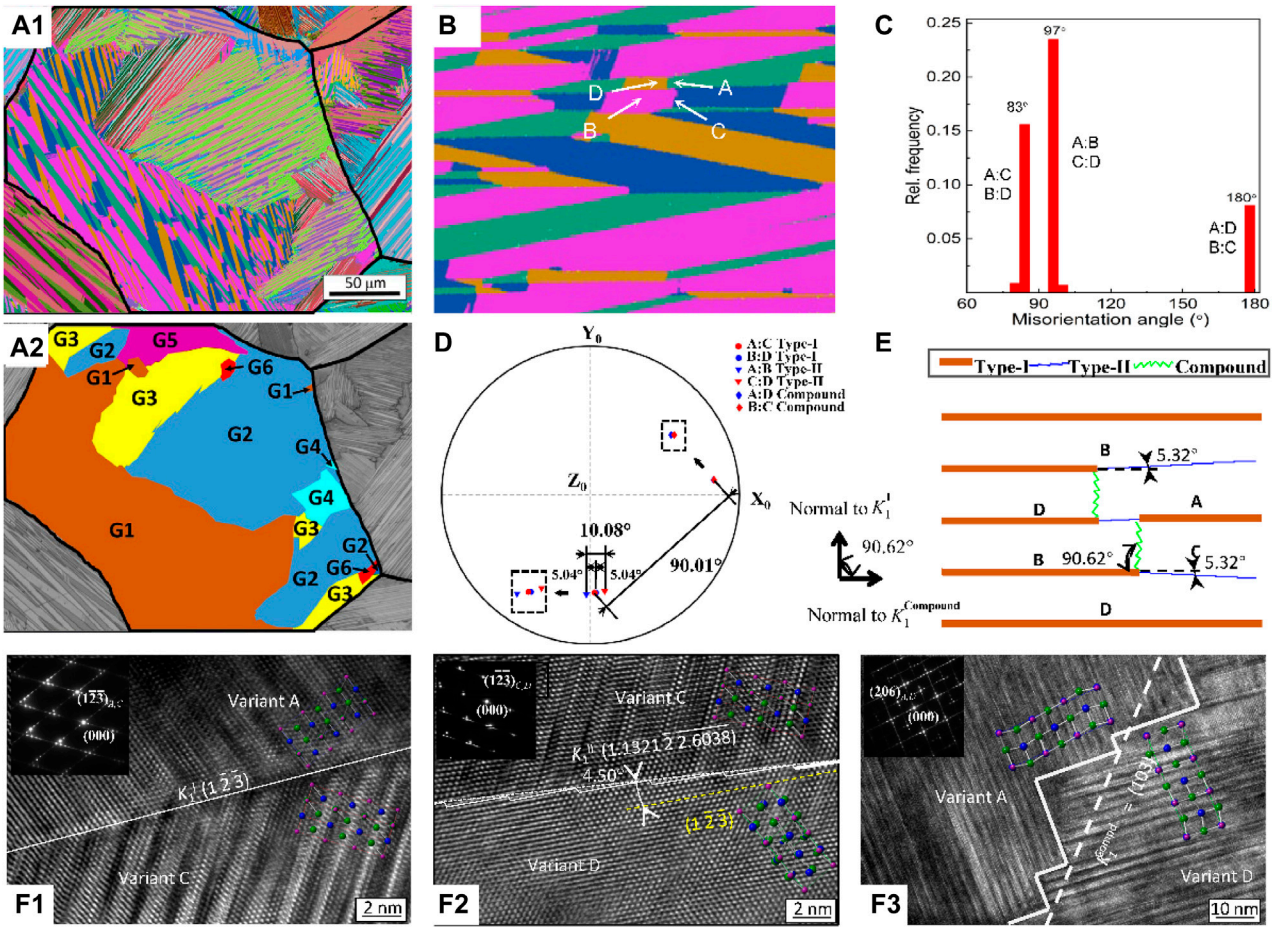

FIGURE 5 | Crystallographic orientation **(A_1)** and variant-group distribution **(A_2)** maps of the 6M modulated martensite of the NiMnIn-based alloys at room temperature measured using SEM/EBSD. The bold black line represents the initial austenite grain. **(B)** Variant organization within the martensite variant group. **(C)** Minimum misorientation angles of different variant pairs. **(D)** Stereographic projections of twinning plane K_1 of different variant pairs. **(E)** 2D illustration of variant organization. High-resolution TEM images of the type-I **(F_1)**, the type-II **(F_2)**, and the compound **(F_3)** twin interfaces (Yan et al., 2016b). Reproduced with the permission of Elsevier Publisher.

(SAED) pattern were acquired and simulated using the determined crystal structure data, as shown in **Figures 4D,E**. It can be seen that both the main and satellite reflections are accurately represented with the established superstructural model.

Recently, by means of synchrotron and neutron diffraction, using the (3+1) dimensional superspace theory, P. Devi et al. also reported that the $Ni_2Mn_{1.4}In_{0.6}$ alloy possesses a 6M incommensurate structure (Devi et al., 2018). It is worth emphasizing that the type of modulated martensite in the NiMn-based alloy is very sensitive to external stress and the sample state. Based on the TEM SAED method, 5M, 7M, and 8M modulated structures (Ito et al., 2007; Liu et al., 2008; Karaca et al., 2009; Erkartal et al., 2012; Huang et al., 2016; Paramanik and Das, 2016) were also observed in the NiMnIn-based alloys. Nevertheless, for the stress-free powder sample investigated by neutron and X-ray diffraction, so far, only the 6M modulated martensite has been evidenced in the Ni(Co)MnIn based alloys.

2.3 Perspectives

(1) The formation mechanism of modulated martensite is still unclear. For the $Ni_2Mn_{1+x}In_{1-x}$ alloy, the martensite has a non-modulated double $L1_0$ structure when the In content is low, while the structure of martensite transforms into a complex long periodic layered 6M modulated structure when the In content is high. Moreover, the NiMnGa-based alloys have 5M and 7M structures, and NiMnSn and NiMnSb alloys possess 4O structure, but only 6M structure is observed in the NiMnIn-based alloys at the stress-free state. As mentioned above, structural modulation often brings excellent magnetoresponsive properties. However, so far, the formation mechanism of modulated structure is still an open issue.

(2) The relationship between the modulated martensite and the functional properties in the NiMn-based alloy is not clear yet. The excellent magnetoresponsive performances of the NiMn-based alloys often only exist in alloys with a modulated martensite structure. However, the quantitative

TABLE 1 | Twining elements of the type-I, the type-II, and the compound twins for the 6M modulated martensite of the NiMnIn alloys (Yan et al., 2016a). K_1, K_2, η_1, η_2, s, and P represent the twinning plane, the conjugate twinning plane, the twinning direction, the conjugate twinning direction, the shear magnitude and the shear plane, respectively. $\omega/\boldsymbol{d}$ indicates the minimum misorientation angle/the corresponding rotation axis, respectively. Reproduced with permission of the International Union of Crystallography.

Twinning elements	Type-I twin A: C, B: D	Type-II twin A: B, C: D	Compound twin A: D, B: C
K_1	$\{1\bar{2}3\}_M$	$\{1.13\,\bar{2}\,\bar{2.60}\}_M$	$\{103\}_M$
K_2	$\{\bar{1}.13\,\bar{2}\,2.60\}_M$	$\{\bar{1}2\bar{3}\}_M$	$\{\bar{1}03\}_M$
η_1	$<\bar{3}.34\,\bar{3}\,0.88>_M$	$<\bar{3}3\bar{1}>_M$	$<\bar{3}01>_M$
η_2	$<3\bar{3}\bar{1}>_M$	$<3.34\,\bar{3}\,\bar{0.88}>_M$	$<301>_M$
P	$\{1\,\bar{0.12}\,3.36\}_M$	$\{1\,0.12\,3.36\}_M$	$\{010\}_M$
s	0.27	0.27	0.03
$\omega/\boldsymbol{d}$	82.40°/ $<301>_M$	97.60°/Normal of $\{103\}_M$	180°/ $<\bar{3}01>_M$

relationship between the modulated structure and the properties has yet to be established.

3 MICROSTRUCTURE OF 6M MODULATED MARTENSITE

3.1 Variant Organization

Based on the established superstructural model (**Figure 4C**), by using the SEM/EBSD technique combined with the orientation analysis method, the morphological and the crystallographic characters of the 6M modulated martensite microstructure of the NiMnIn alloys were characterized in detail (Yan et al., 2015; Yan et al., 2016b; Yan et al., 2016c; Yan et al., 2021b). Experiments showed that the 6M modulated martensite is in a plate shape and self-organized in colonies, as shown in **Figure 5A$_1$**. Within one initial austenite grain, a maximum of 6 orientation-independent variant colonies (**Figure 5A$_2$**) and a total of 24 orientation-independent variants can be generated. The formation mechanism of the microstructure will be discussed with the transformation strain path in **Section 4**. In each martensite colony, as shown in **Figure 5B**, there are four orientation variants, i.e., A, B, C, and D.

Misorientation examinations showed that the four variants within the martensite colony are twin-related. In total, there exist three types of twins, i.e., type-I (A: C and B: D), type-II (A: B and C: D), and compound (A: D and B: C) twins (Yan et al., 2016b). The twinning elements of K_1, K_2, η_1, η_2, s, and P for different types of twins, determined with the method proposed by Zhang et al. (2010), are listed in **Table 1**. It is seen that the shear magnitudes of the type-I and the type-II twins are the same (0.27), which is around one order of magnitude larger than that of the compound twin (0.03). Misorientation calculations showed that for the 6M NiMnIn modulated martensite, the theoretical angle/axis pair ($\omega/\boldsymbol{d}$) for the type-I, the type-II, and the compound twins are 82.4°/ $<301>_M$, 97.6°/normal of $\{103\}_M$ and 180°/ $<\bar{3}01>_M$ (Yan et al., 2016c), respectively, which is in good agreement with the experimental measurements (**Figure 5C**).

3.2 Twin Interface Structure

Twin boundary is a key material parameter that significantly affects both the physical and mechanical properties of materials. For the 6M modulated martensite of the NiMnIn alloys, using the indirect two-trace method (Zhang et al., 2007), the interface indices between different variants within the martensite colony are found to coincide with their twinning plane K_1 in the mesoscale (Yan et al., 2016a). Within one martensite colony, as shown in **Figure 5D**, there is only one kind of type-I (indicated by the solid circle) and compound twin (indicated by the solid diamond) boundaries. In other words, the two boundaries between the type-I twin related variants A: C and B: D (or the compound twin related variants A: D and B: C) are parallel to each other. In addition, the interface between the type-I twin related variants is almost perpendicular to the interface between the compound twin related variants. In contrast, the two boundaries between the type-II twin related variants (indicated by the inverted triangle), i.e., the interfaces between A: B and C: D, are separated. It is seen from **Figure 5D** that the two kinds of type-II twin interfaces are distributed on the two sides of the type-I twin interfaces with an angle of around 5°. The orientation characters of various interfaces within one martensite colony are illustrated in **Figure 5E**.

High-resolution TEM characterization showed that at the atomic scale, the type-I twin interface possesses a straight boundary, whereas the type-II twin boundary has a "stepped" interface (Yan, et al., 2016a). This difference leads to much smaller detwinning stress of the type-II twin with respect to that of the type-I twin, although the shear magnitudes of these two twins are exactly the same. For the compound twin, even though its twinning plane is rational, i.e., $\{103\}_M$, it also has a "stepped" interface at the atomic scale. Compared with the type-II twin, the step of the compound twin is much larger and shows an irregular distribution feature. The irregularly stepped interface structure and the small shear of the compound twin account for its high mobility (Yan et al., 2016a).

3.3 Perspectives

The reason for the difference in detwining stress of different twin systems is still unclear. For the modulated martensite, there are huge differences in the detwining stresses for type-I, type-II, and compound twin systems. At present, we can only speculate that this phenomenon is related to the magnitude of the shear and the structure of the interface. However, the underlying physical mechanism still needs to be explored.

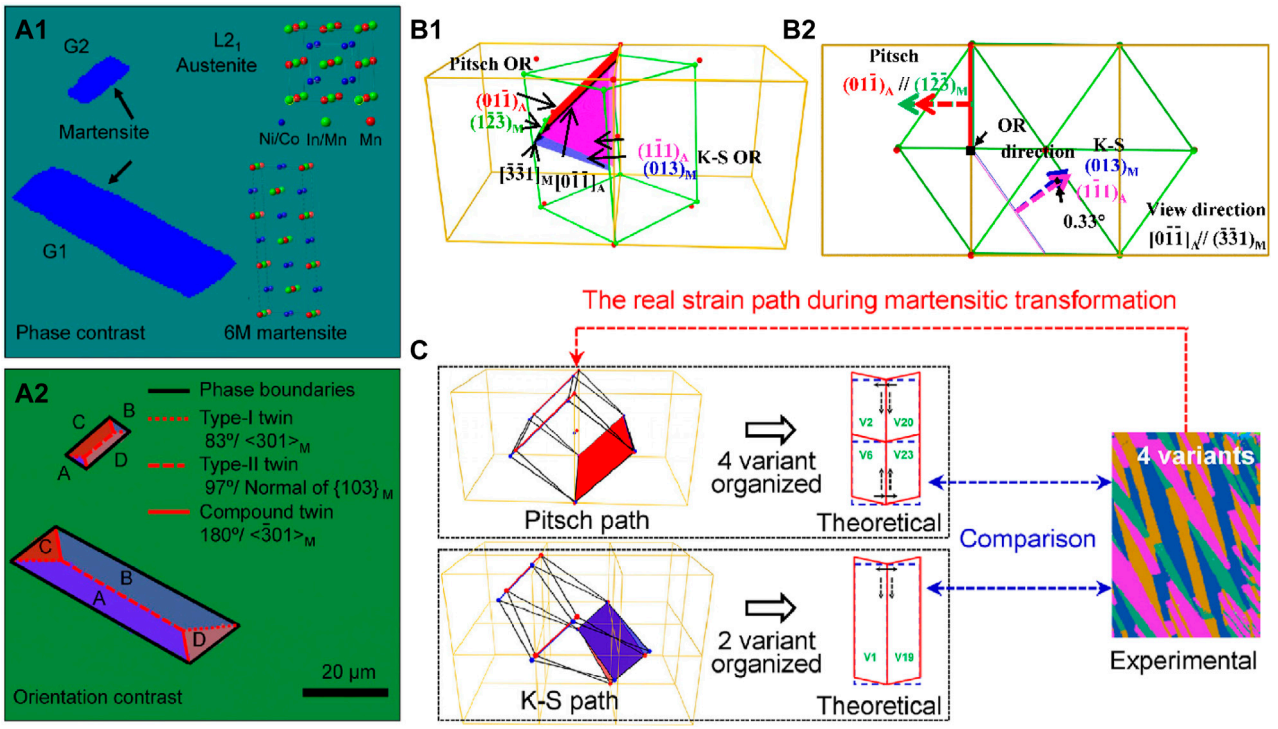

FIGURE 6 | Phase contrast **(A_1)** and crystallographic orientation **(A_2)** maps of the dual-phase $Ni_{45}Co_5Mn_{36.8}In_{13.2}$ alloy measured by using the SEM/EBSD technique at room temperature. **(B_1)** Geometrical relation between the K-S and the Pitsch orientation relationships (ORs). **(B_2)** is the projection of (B_1) along the OR direction. **(C)** Basic idea of determining transformation strain path based on the variant organization of martensite variants. Reproduced with the permission of Elsevier Publisher.

4 CRYSTALLOGRAPHY OF MARTENSITIC TRANSFORMATION

The magnetoresponsive behaviors of the NiMnIn-based alloys are closely related to the magnetic field-induced inverse martensitic transformation. It is thus greatly meaningful to clarify the crystallographic characteristics of martensitic transformation, including transformation orientation relationship (OR), transformation strain path, etc., to understand the formation mechanism of microstructure and magnetoresponsive behaviors.

4.1 Transformation Orientation Relationship

Transformation OR describes the geometrical relation between the crystal lattices of austenite and martensite. Generally, the transformation OR is represented by plane and in-plane direction correspondences, i.e., $\{hkl\}_A//\{hkl\}_M$ and $<uvw>_A//<uvw>_M$ where the subscript "A" and "M" represent austenite and martensite, respectively. By composition design, a dual-phase $Ni_{45}Co_5Mn_{36.8}In_{13.2}$ alloy at room temperature was fabricated, and the accurate crystallographic orientations of the two coexisting phases were measured by using the SEM/EBSD technique (Yan et al., 2021a), as shown in **Figure 6A**. With the orientation information of the co-existing austenite and martensite, the reported ORs in the literature, including the Bain (Bain and Dunkirk, 1924), the Nishiyama-Wassermann (N-W) (Nishiyama, 1934), the Kurdjumov-Sachs (K-S) (Kurfib and Schultz, 1930), and the Pitsch (Pitsch, 1962) ORs were examined one by one. Results showed that the deviations of the measured misorientation between austenite and martensite Δg^{exp} from the theoretical Δg^{OR} of the Bain, the N-W, the K-S, and the Pitsch ORs are 3.73°, 1.27°, 0.70°, and 0.63° (Yan et al., 2021a), respectively.

For the Bain and the N-W ORs, the deviation angles are the largest (>1°), and thus these two ORs can be excluded. In contrast, for both the K-S and the Pitsch OR, the deviation angles are both the smallest and are close to the angular resolution of current EBSD technology (±0.5°). Thus, it is difficult to discriminate which is the valid OR or to determine that both are valid. It is worth emphasizing that such a dual OR occasion is not a unique occurrence in the studied $Ni_{45}Co_5Mn_{36.8}In_{13.2}$ alloy nor in the NiMnIn-based alloys. This dual-OR phenomenon widely exists in many other NiMn-based ferromagnetic shape memory alloys with modulated martensite, such as $Ni_{50}Mn_{30}Ga_{20}$ (Li Z. B. et al., 2011) with 7M modulated martensite, $Ni_{50}Mn_{28}Ga_{22}$ (Li Z. et al., 2011) with 5M modulated martensite and $Ni_{50}Mn_{38}Sb_{12}$ (Zhang et al., 2016) alloy with 4O modulated martensite.

In order to reveal the difference between the K-S and the Pitsch OR in the NiMnIn-based alloys, the correspondent crystalline planes and crystalline directions of these two ORs are outlined in the austenite (orange) and the martensite (green) lattices that strictly obey the Pitsch OR, as shown in **Figure 6B$_1$**. It

is seen that the OR directions of the K-S and the Pitsch relations are exactly the same. The difference between these two ORs lies in the OR planes. For the K-S relation, the OR plane pair is $\{111\}_A//\{013\}_{6M}$, while the OR plane pair of Pitsch relation is $\{101\}_A//\{1\overline{2}3\}$. **Figure 6B$_2$** is a projection of **Figure 6B$_1$** along the OR direction (the black arrow), i.e., $[0\overline{1}\overline{1}]_A$. The normal of the OR plane in **Figure 6B$_2$** is indicated by the dotted line. It is seen from **Figure 6B$_2$** that when the Pitsch OR is strictly satisfied, for the K-S relation, the deviation between the OR planes of austenite and martensite is just 0.33° away. From the point of view of geometry, this is the difference between the K-S and the Pitsch OR. The reason that the K-S and the Pitsch OR are almost simultaneously satisfied could be related to the special lattice parameters of austenite and martensite in the NiMn-based alloys. The underlying physical mechanism still needs to be further studied.

4.2 Transformation Strain Path

By definition, the transformation OR of martensitic transformation describes the geometric relation between the crystal lattices of austenite and martensite. Nevertheless, considering that the martensitic transformation involves a shear process and the atomic displacement during this process is far less than one atomic spacing, the OR plane $\{hkl\}_A$ and OR direction vector $[uvw]_A$ of austenite should not rotate (distortion is allowed) during the lattice distortion of phase transformation. Thus, OR can be used to describe the transformation strain path of martensitic transformation, that is, the OR plane $\{hkl\}_A$ of austenite shears along the OR direction $<uvw>_A$. It is worth emphasizing that the OR plane of austenite $\{hkl\}_A$ is not the so-called habit plane since both rotation and distortion are not allowed for the habit plane, but only rotation is forbidden for the OR plane. During the lattice distortion of martensitic transformation, the OR plane {hkl} and the OR direction <uvw> can be distorted to realize the change of crystal structure.

Normally, the transformation strain path can be easily obtained from the transformation OR. However, for the NiMnIn-based alloys, both the K-S and the Pitsch ORs can be approximately satisfied. Thus, the commonly utilized method to determine the transformation strain path through the relevant orientation relationship is no longer applicable. For the NiMnIn-based alloys, from the viewpoint of transformation OR, the conclusion that can be drawn is that the two transformation strain paths, i.e., the K-S type $\{1\ \overline{1}\ 1\}_A<0\ \overline{1}\ \overline{1}>$ and the Pitsch type $\{01\ \overline{1}\}_A<0\ \overline{1}\ \overline{1}>$ (**Figure 6C**) may occur. Previous studies showed that the martensitic transformation occurs at the speed of sound (Bunshah and Mehl, 1953; Mukherjee, 1968), so the direct determination of the transformation strain path is difficult even by using modern physical characterization techniques.

Usually, the resultant behaviors of phase transition are greatly affected by the transformation process. Thus, one can assume that the microstructure characters of martensite produced by different transformation strain paths are likely to be different. Based on this assumption, a strategy of determining the transformation strain path was proposed, i.e., deducing the transformation strain path according to the microstructural features of martensite (Yan et al., 2021b). With this strategy, the transformation strain path of NiMnIn alloy was determined successfully. To satisfy the criterion of the minimum interface and elastic strain energies, combined with the stress and the strain compatibility conditions, theoretically, the K–S path produces two variants as a self-accommodated variant group, whereas the Pitsch path produces four variants as a self-accommodated variant group, as shown in **Figure 6C**. The details are referred to Ref. (Yan et al., 2021a). For the NiMnIn-based alloy, as shown in **Figure 5B** and **Figure 6A**, the self-accommodated variant group is composed of 4 orientation variants. Thus, the Pitsch strain path, $\{01\ \overline{1}\}_A<0\ \overline{1}\ \overline{1}>_A$, was evidenced to be the real one that governs the lattice distortion during martensitic transformation.

Moreover, it is found that the 4 self-accommodated martensite variants within the variant group are transformed on the same transformation plane $\{01\ \overline{1}\}_A$ (Yan et al., 2021b). For example, all 4 self-accommodated martensitic variants A, B, C, and D in **Figure 6A$_2$** are transformed mainly by shear deformations on the same $(10\ \overline{1})_A$ plane. The transformation strain paths for these 4 variants lies just by permutating the signs (positive or negative) of the transformation plane and direction. For instance, the specific transformation strain paths for A, B, C, and D are $(10\ \overline{1})_A[101]_A$, $(\overline{1}\ 01)_A[101]_A$, $(10\ \overline{1})_A[\overline{1}\ 0\ \overline{1}]_A$, and $(\overline{1}\ 01)_A[\overline{1}\ 0\ \overline{1}]_A$, respectively. During the martensitic transformation process, the 4 self-accommodated variants gradually grow and develop into a martensite variant group. For cubic structure, owing to the crystal symmetry, there are 6 equivalent Pitsch-type transformation planes $\{01\ \overline{1}\}_A$, i.e., $(01\ \overline{1})_A$, $(011)_A$, $(10\ \overline{1})_A$, $(101)_A$, $(1\ \overline{1}0)_A$, and $(110)_A$. Therefore, theoretically, an austenite grain can form a maximum of 6 independent variant groups and in total 24 orientation-independent variants. This result is consistent with the experimental observation (**Figure 5A**) and explains well the formation mechanism of the self-accommodated microstructure of 6M modulated martensite of the NiMnIn alloys.

4.3 Perspectives

The underlying physical mechanism why the K-S and the Pitsch transformation orientation relations are almost simultaneously satisfied in the NiMn-based alloys is still unclear. The shuffling path of the different $(001)_M$ atomic layers during the martensitic transformation is still unclear. The Pitsch-type transformation strain path can only reveal the shear mode of the average lattice of modulated martensite. However, in addition to the Pitsch-type lattice distortion, the shuffling of the $(001)_M$ atomic layer is also needed to form the modulated martensite. The physical mechanism of this process is still unclear.

5 MAGNETIC SHAPE MEMORY EFFECT

NiMnIn-based alloys can achieve the shape memory effect *via* the magnetic-field-induced inverse martensitic transformation from the weak-magnetic martensite to the ferromagnetic austenite, which is called the magnetic shape memory effect (MSME). The mechanism of MSME of the NiMnIn-based alloys is illustrated in **Figure 7**. When the pre-deformed martensite of a NiMnIn alloy is exposed in a magnetic field, at the condition that the driving force

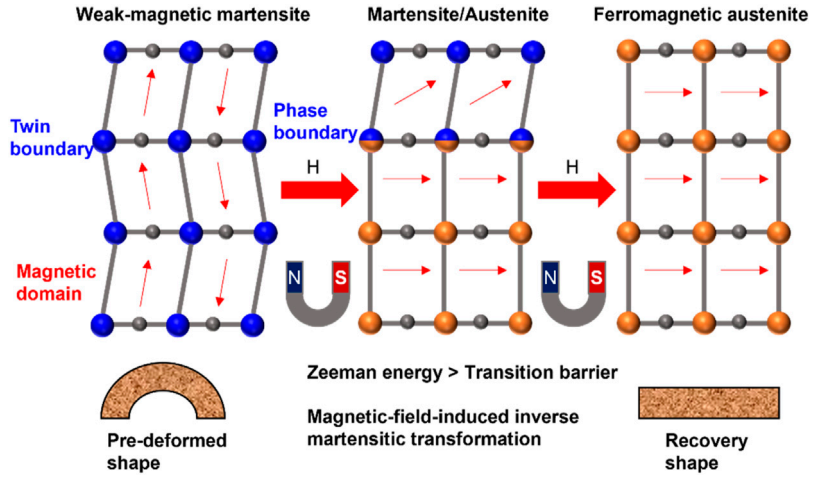

FIGURE 7 | Schematic diagram of magnetic shape memory effect (MSME) from the weak-magnetic martensite to the strong-magnetic austenite.

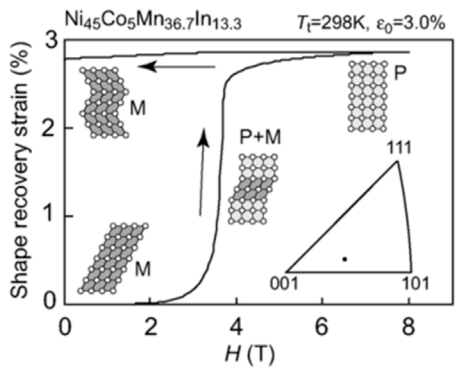

FIGURE 8 | Magnetic shape memory effect (MSME) in the single-crystalline $Ni_{45}Co_5Mn_{36.7}In_{13.3}$ alloy measured at room temperature (Kainuma et al., 2008). Reproduced with the permission of Royal Society of Chemistry Publisher.

for the inverse martensitic transformation (the Zeeman energy difference, $\mu_0 H\Delta M$) exceeds the energy barrier of structural transition, the new phase of austenite nucleates and grows, and thus resulting in the shape recovery (Karaca et al., 2007). Compared with the conventional thermally-induced SME that is limited by the low heat conduction rate, the MSME of the NiMnIn-based alloys shows the advantages of fast response, easy control, and high stability. Moreover, different from NiMnGa in which the magnetic output work (magneto-stress) is limited by the magnetocrystalline anisotropy energy (Karaca et al., 2006; Karaca et al., 2007), the magneto-stress of the NiMnIn-based alloys continuously increases with the strength of magnetic field as there is no limit for the Zeeman Energy (Karaca et al., 2009; Turabi et al., 2016).

In 2006, for the first time, R. Kainuma et al. reported the MSME in a Co-doped $Ni_{45}Co_5Mn_{36.7}In_{13.3}$ single-crystalline sample (Kainuma et al., 2006). They observed that a pre-strain of 3% can almost be recovered by the magnetic field-induced inverse martensitic transformation in the $Ni_{45}Co_5Mn_{36.7}In_{13.3}$ single-crystalline sample, as shown in **Figure 8**. Based on the Clausius–Clapeyron relation, the output magneto-stress generated during the transformation was estimated to be about 108 MPa under a magnetic field of 7 T (Kainuma et al., 2006), which is about 50 times larger than that of NiMnGa (2 MPa) (Murray et al., 2000). Later, under a pulsed magnetic field of 70 kOe, a 3% recoverable strain was obtained in the $Ni_{45}Co_5Mn_{36.7}In_{13.3}$ single-crystalline sample at room temperature (Sakon et al., 2007). Since then, the MSME of the NiMnIn-based alloys has attracted more and more attention.

For the MSME, in view of practical applications, a large magnetic-field-induced strain (MFIS) is desirable (Jiang et al., 2013; Barua et al., 2018). For the NiMnIn-based alloys, owing to the high energy barrier, the magnitude of MFIS is closely associated with the transformed volume under an external magnetic field, which is greatly affected by the sensitivity of transformation temperature to the magnetic field, i.e., $\Delta T/\Delta H$. Normally, under a given magnetic field, a large $\Delta T/\Delta H$ tends to increase the transformed volume and thus the magnitude of the MFIS. Besides, a large $\Delta T/\Delta H$ can expand the operating temperature window of the MSME. Based on the Clausius–Clapeyron relation (**Eq. 1**),

$$\frac{\Delta T}{\Delta H} = \frac{\Delta M}{\Delta S} \tag{1}$$

where ΔM and ΔS represent the magnetization difference and the entropy change during the martensitic transformation, respectively, it is clear that a large ΔM value is favorable to promote a high magnetic-field sensitivity of transformation temperature ($\Delta T/\Delta H$). So far, for the NiMnIn-based alloys, the most successful strategy of increasing ΔM is the partial substitution of Co for Ni. Thus, the MSME of the Co-doped NiCoMnIn alloys has been intensively studied (Karaca et al., 2009; Monroe et al., 2012; Turabi et al., 2016; Bruno et al., 2017).

5.1 NiCoMnIn

Like the conventional shape memory alloy, for the single crystal sample, since the counteraction of transformation strains generated by different austenite grains with distinct orientations is avoided, the transformation strain is much larger than that of the polycrystalline sample. Thus, studies on the MFIS in the NiMnIn-based alloys were first focused on single crystals. Under a magnetic field of 18 T and bias stress of 125 MPa, J.A. Monroe and cooperators observed a fully recoverable transformation strain of 3.1% in the <100> oriented $Ni_{45}Co_5Mn_{36.5}In_{13.5}$ single crystal (Monroe et al., 2012). For this sample, an output work of 1 MJ m^{-3} T^{-1} (Karaca et al., 2009) and a magneto-stress of 71 MPa at a magnetic field of 9 T (Turabi et al., 2016) were obtained. Both of them are one order of magnitude higher than those in NiMnGa. The theoretical magneto-stress along [100], [123], [011], and [111] were 26.5, 42.2, 50.4, 143.4 MPa T^{-1}, respectively, which are much larger than the corresponding values in NiMnGa (2–5 MPa T^{-1}). Along the [111] direction, a transformation strain of ~1.2% was observed. N. M. Bruno et al. found that the magneto-mechanical training can significantly reduce the critical magnetic field required for the inverse martensitic transformation from 8.3 T to 1.3 T in the single-crystalline $Ni_{45}Co_5Mn_{36.6}In_{13.4}$ alloy (Bruno et al., 2017). After the magneto-mechanical training, under a magnetic field of 3 T, an MFIS of 5.6% was obtained.

Apart from single crystals, owing to the simple preparation process and the low cost, the MSME of the NiMnIn-based polycrystalline alloys were also studied (Krenke et al., 2007; Liu et al., 2009a; Sharma et al., 2010a; Li et al., 2010; Acet et al., 2011; Yu et al., 2014; Yu et al., 2016), although the magnitude of the MFIS of polycrystalline sample is generally smaller than those of single crystals. In 2007, by using *in-situ* X-ray diffraction technology, Y. D. Wang et al. evidenced the occurrence of magnetic-field-induced reversible martensitic transformation in the $Ni_{45}Co_5Mn_{36.6}In_{13.4}$ polycrystalline sample under a uniaxial compressive stress of 50 MPa and a magnetic field of 5 T (Wang et al., 2007). In 2009, J. Liu et al. studied the MFIS of the textured $Ni_{45.2}Mn_{36.7}In_{13}Co_{5.1}$ polycrystalline sample during two magnetic-field cycles at 310 K (Liu et al., 2009b). They found that magnetic training was able to enhance the magnitude of magnetostrain from 0.2% (the first magnetic cycle) to 0.25% (the second magnetic cycle). After the magnetic training, the critical magnetic field of transformation is reduced from 1.6 T to 1.2 T. In 2010, Z. Li et al. found that the non-prestrained $Ni_{45}Co_5Mn_{37}In_{13}$ polycrystalline alloy possesses a reversible MFIS of 0.4% and exhibits a large two-way MSME without applying a pre-strain (Li et al., 2010). Moreover, the two-way MSME was still reproducible even after three magnetic-field cycles at 320 K.

5.2 Other NiMnIn-Based Alloys

Apart from the Co-doped NiCoMnIn, the MSME of undoped (Krenke et al., 2007), Cu-doped (Sharma et al., 2010b), Sb-doped (Yu et al., 2014), and Ga-doped (Yu et al., 2016) NiMnIn-based polycrystalline samples were also studied. In 2007, T. Krenke and collaborators obtained an MFIS of 0.12% under a magnetic field of 5 T in the ternary $Ni_{50}Mn_{34}In_{16}$ polycrystalline sample (Krenke et al., 2007). Later, S. Y. Yu et al. found that the transformation strain increases rapidly with the doping by Sb (Yu et al., 2014). Under a magnetic field of 10 T, an MFIS of 1.7% was obtained in the non-prestrained $Ni_{50}Mn_{36}In_8Sb_6$ alloy (Yu et al., 2014). Unfortunately, the critical magnetic field in this alloy is as large as ~ 6 T, and there is almost no shape recovery after removing the magnetic field. Besides, by using the directional solidification technique, S. Y. Yu et al. obtained an MFIS of −0.28% along (and 0.49% perpendicular to) the solidification direction in the polycrystalline $Ni_{50}Mn_{33}In_{13}Ga_4$ alloy (Yu et al., 2016).

5.3 Perspectives

For the NiMnIn-based alloys, both the single-crystal and the polycrystalline samples have excellent MSME, which makes this compound a potential candidate for smart sensors and actuators. However, in view of commercial application, there are still some thorny problems that need to be solved:

High critical magnetic field required to drive reversible transformation. Usually, the critical magnetic field required to drive a completely reversible transformation in the NiMnIn-based alloys is as large as ~ 3 T (Kainuma et al., 2006; Li et al., 2010; Huang et al., 2021), which greatly limits the application range of this compound. For instance, the critical magnetic fields for the inverse martensitic transformation in the $Ni_{45}Co_5Mn_{37}In_{13}$ alloy at 320 K and 310 K are as large as 5 T and 7 T, respectively (Li et al., 2010).

Large thermal hysteresis ΔT_{hys} and transition interval ΔT_{int} during martensitic transformation. The large thermal hysteresis ΔT_{hys} and transition interval ΔT_{int} may lead to the retain of partial austenite after removing the magnetic field and ultimately reduce the transformed volume fraction. For instance, due to the existence of thermal hysteresis, the value of MFIS in the $Ni_{50}Mn_{36}In_8Sb_6$ alloy becomes irreversible after removing the magnetic field (Yu et al., 2014).

Based on the previous studies, for the NiMnIn-based alloys, the critical magnetic field, thermal hysteresis, and transition interval could be optimized in the following ways:

a) External field training to reduce the critical magnetic field. The external field training methods, such as mechanical, magnetic, and thermo-mechanical training, can reduce the number of martensite variants. After that, the number of unfavorable variants is reduced by the process of detwinning (Yan et al., 2016a), and thus the critical magnetic field driving the inverse martensitic transformation can be reduced.
b) Applying mechanical or thermal field to reduce thermal hysteresis and critical magnetic field. Generally speaking, for the NiMnIn-based alloys, the mechanical field stabilizes the martensite, and the thermal field stabilizes the austenite. Applying the mechanical or the thermal field reasonably to assist transformation can reduce the thermal hysteresis and the critical magnetic field of MSME.
c) Increasing geometrical compatibility between austenite and martensite to reduce thermal hysteresis. Adjusting the lattice parameters of austenite and martensite by tailoring the

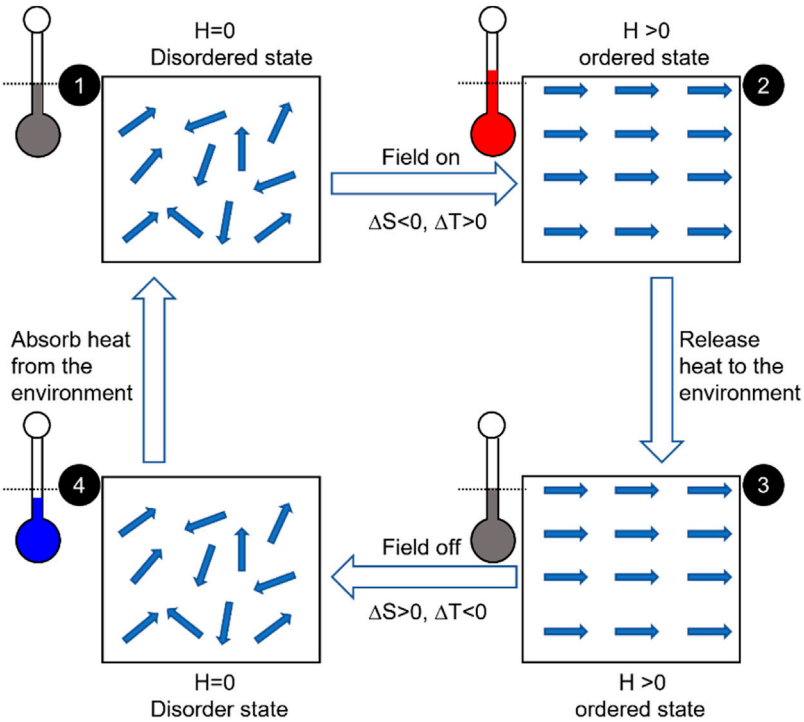

FIGURE 9 | Schematic diagram of magnetocaloric effect for the conventional materials.

chemical composition to increase the geometric compatibility between austenite and martensite can reduce the thermal hysteresis.

d) Tailoring microstructural features to control thermal hysteresis. The microstructure characteristics, including grain boundary, point defect, and phase constituent, play important roles in the nucleation and growth of martensite. Thus, the hysteresis can also be tuned by microstructure modification.

Reasonably utilizing the above-mentioned strategies, it is possible to significantly improve the MSME of the NiMnIn-based alloys and thus promote the practical application of this compound in the field of smart sensors and actuators.

6 MAGNETOCALORIC EFFECT

The magnetocaloric effect (MCE) refers to the temperature change ΔT of a material when exposed to an external magnetic field (Wiedemann, 1889; Moya et al., 2014). Nowadays, the magnetocaloric refrigeration technique has been successfully applied in the low and extremely low-temperature refrigeration fields, such as physical property measurement, superconducting environment, and cryogenic physics, and shows the potential of entering the conventional room-temperature refrigeration market (Yu et al., 2010; Kitanovski and Egolf, 2009), such as conditioner, refrigerator, and food freezer. Generally, the MCE is characterized by the isothermal magnetic entropy change ΔS_M or the adiabatic temperature change ΔT_{ad}. The mechanism of MCE in the conventional materials is shown in **Figure 9**. When a magnetic material is exposed to a magnetic field, the magnetic moment tends to be parallel to the direction of the applied magnetic field, resulting in a decrease in magnetic entropy and thus a rise in temperature. By heat exchange, the heat of the MCE material releases into the environment. When the magnetic field is removed, the magnetic moments of magnetic atoms tend to be disordered again due to the thermal vibration, resulting in an increase in magnetic entropy and a decrease in temperature. In 1933, by using the thermal-magnetic cycle illustrated in **Figure 9**, W. F. Giauque and D. P. Macdougall successfully realized an ultra-low temperature of 0.25 K by using the paramagnetic salt $Gd_2(SO_4)_3{\cdot}8H_2O$ (Giauque and Macdougall, 1933). Subsequently, a variety of excellent low-temperature magnetic refrigerants have been discovered, such as $Gd_2(SO_4)_3{\cdot}8H_2O$ (Giauque and Macdougall, 1933), GGG ($Gd_3Ga_5O_{12}$) (McMichael et al., 1993), and RAl_2 (R = Er, Ho, Dy, $Dy_{0.5}Ho_{0.5}$, Dy_xEr_{1-x}, Gd and Pd) (Hashimoto et al., 1987). After the development of the low-temperature magnetic refrigerants for half a century, in 1976, G. V. Brown observed a room-temperature MCE effect in Gd (Brown, 1976). At this time, both the low-temperature and the room-temperature MCE effects were realized at around the temperature of the second-order Cuire magnetic transition.

A breakthrough came in 1997. In this year, V. K. Pecharsky and K. A. Gschneidner et al. reported a first-order phase transition related room-temperature magnetocaloric material

$Gd_5Si_2Ge_2$ (Pecharsky and Gschneidner, 1997). In this material, a giant ΔS_M of about 18 J kg^{-1} K^{-1} under a magnetic field of 5 T was obtained at 280 K, which is about twice larger than that of Gd. Further investigations showed that this large ΔS_M comes from the magnetic-field-induced transformation from the paramagnetic monoclinic phase to the ferromagnetic orthorhombic phase. From then on, the magnetocaloric materials associated with the first-order phase transition attracted great attention based on this work.

For the NiMnIn-based alloys, as mentioned above, the martensitic transformation is accompanied by significant changes in magnetism, which is similar to the case of $Gd_5Si_2Ge_2$ (Pecharsky and Gschneidner, 1997). Thus, since the discovery of NiMnIn alloy, the magnetocaloric effect of this compound has attracted increasing attention. By the Maxwell relation, R. Kainuma et al. found that the $Ni_{45}Co_5Mn_{36.7}In_{13.3}$ single-crystal exhibits a large ΔS_M of 28.4 J kg^{-1} K^{-1} at 292 K under a magnetic field of 7 T (Kainuma et al., 2006). This value of ΔS_M is comparable to the famous room-temperature rare-earth-based MCE refrigerant, such as $Gd_5Si_2Ge_2$, MnAsSb, and La(Fe, Si)13. Besides, since the critical temperature of first-order martensitic transformation can be easily tailored by composition modification, the NiMnIn-based alloy has adjustable refrigeration working temperature, as well as relatively low cost, compared with the second-order Cuire transition associated rare-earth-based MCE materials, such as Gd, RAl_2 (R = Er, Ho, Dy, $Dy_{0.5}Ho_{0.5}$, Dy_xEr_{1-x}, Gd and Pd), RE-TM (RE = Nd, Ho, Er, and Tm; TM = Zn and Ga) and RETMX (RE = Tb, Dy, Ho, and Er; TM = Fe, Co, and Pt; X = Al, Mg, and C) (Luo and Wang, 2009; Nirmala et al., 2015; Li and Yan, 2020). Moreover, different from the conventional MCE refrigerants in which the temperature is increased upon the application of magnetic field, the temperature of the NiMnIn-based alloys is decreased when a magnetic field is applied. For the NiMnIn-based alloys, when a magnetic field is applied, the heat absorbed from the structural transition from the low-entropy martensite phase to high-entropy austenite is larger than the heat released from the alignment of magnetic moments during the process of the inverse martensitic transformation. Therefore, the temperature of the sample decreases during the process of the magnetic-field induced inverse martensitic transformation. Clearly, the MCE in the NiMnIn-based alloys is different from the above-mentioned conventional magnetocaloric effect, which thus is termed as the inverse magnetocaloric effect (Tegus et al., 2002; Krenke et al., 2005).

For the MCE refrigerant, the following requirements should be satisfied: 1) the value of isothermal magnetic entropy change ΔS_M (or adiabatic temperature change ΔT_{ad}) should be as large as possible as it directly decides the refrigeration efficiency; 2) the transition thermal hysteresis ΔT_{hys} accompanied with the magnetostructural transformation should be as small as possible since the existence of large thermal hysteresis will greatly reduce the cooling efficiency and may further cause the functional fatigue after several cycles; 3) the refrigeration temperature window δT_{FWHM} should be as wide as possible. Aimed at improving the above-mentioned three parameters, the MCE of the NiMnIn-based alloys has been extensively studied during the past 15 years. Next, the main progress related to the improvement of ΔS_M (or ΔT_{ad}), ΔT_{hys}, and δT_{FWHM} in the NiMnIn-based alloys will be briefly reviewed.

6.1 Isothermal magnetic Entropy Change

As mentioned above, the isothermal magnetic entropy change ΔS_M (or adiabatic temperature change ΔT_{ad}) is the key parameter to decide the refrigeration capacity for the MCE refrigerants. Thus, to improve ΔS_M or ΔT_{ad}, several strategies, including increasing transformed volume fraction *via* enlarging the driving force of magnetic-field-induced inverse martensitic transformation, reducing the negative contribution of magnetic entropy change ΔS_{mag} to transformation entropy change ΔS_{tr} and exploiting multicaloric effect, have been proposed.

a) Increasing transformed volume fraction *via* increasing the driving force of magnetic-field-induced inverse martensitic transformation. For the NiMnIn-based alloys, one of the critical issues is the high magnetic field requirement to induce a completely inverse martensitic transformation. This results in a limited volume of inverse martensitic transformation under a relatively low magnetic field. In this case, the corresponding MCE performance is significantly reduced compared with that of a complete transformation. This is why the reported MCEs of the NiMnIn-based alloys in the literature were mostly measured with high magnetic field strength, usually 5T (Liu et al., 2009b; Wang et al., 2020; Yang et al., 2020; Bai et al., 2021). It is known that the maximum magnetic field produced by the ordinary permanent magnets is around 2T. This value is much lower than the magnetic field required to induce a complete inverse martensitic transformation in the NiMnIn alloys. Thus, increasing transformed volume under a relatively low magnetic field should be the most efficient method to increase the MCE refrigeration efficiency.

For the NiMnIn-based alloys, the driving force of magnetic-field induced inverse martensitic transformation comes from the giant magnetization difference between austenite and martensite, i.e., Zeeman energy, $\mu_0 H\Delta M$. Thus, under a constant magnetic field, increasing the magnetization difference between austenite and martensite ΔM can greatly elevate the Zeeman energy and thus increase the transformed volume. For the NiMnIn-based alloys, the magnetization of martensite is very small, and thus ΔM is mainly decided by the magnetization of austenite. Therefore, the most effective method to increase ΔM is to enhance the magnetism of austenite.

So far, the most successful method of enhancing the magnetism of austenite in the NiMnIn alloys is the partial substitution of Co for Ni (Kainuma et al., 2006; Liu Z. H. et al., 2009; Pathak et al., 2010; Guillou et al., 2012; Li et al., 2018; Wang et al., 2020; Yang et al., 2020; Bai et al., 2021). In the Co-doped $Ni_{45.2}Mn_{36.7}In_{13}Co_{5.1}$ alloy, J. Liu et al. realized a ΔT_{ad} of −6.2 K under a relatively low magnetic field of 1.9 T at 317 K (Liu et al., 2012). Besides, by using a pulsed magnetic field of 15 T, T. Kihara and collaborators realized a giant ΔT_{ad} of −12.8 K in the $Ni_{45}Co_5Mn_{36.7}In_{13.3}$ alloy (Kihara et al., 2014). Apart from the

doping with Co, Z. H. Liu et al. reported that the addition of Sb can also enhance the ferromagnetism of austenite, thus improving $\Delta T/\Delta H$ (Liu et al., 2009b). In the $Ni_{48.3}Mn_{36.1}In_{10.1}Sb_{5.5}$ alloy, an ΔS_M of 21 J kg^{-1} K^{-1} was obtained at a magnetic field of 5 T (Liu et al., 2009a). Different from the strategy of increasing magnetism of austenite, V. Sánchez-Alarcos reported that the magnetization of martensite can be reduced with the addition of Ti, which further results in an enhancement of MCE (Sánchez-Alarcos et al., 2015).

b) Reducing the negative contribution of magnetic entropy change during the magnetostructural transition. For the MCE associated with the first-order phase transition, the upper-limit of the isothermal magnetic entropy change ΔS_M is the transformation entropy change ΔS_{tr} during phase transition. Thus, a large ΔS_{tr} is a prerequisite to realizing a significant MCE performance. Theoretically, the transformation entropy change ΔS_{tr} comes from three contributions, i.e., the lattice vibration entropy change ΔS_{vib}, the magnetic entropy change ΔS_{mag} and the electronic entropy change ΔS_{elec} (Recarte et al., 2010; Recarte et al., 2012; Wang et al., 2017). For the NiMnIn-based alloys, during the process of magnetic-field induced inverse martensitic transformation from low-entropy martensite to high-entropy austenite, the lattice vibration entropy change ΔS_{vib} is increased. This term makes the highest contribution to ΔS_{tr}. Nevertheless, since the austenite has a highly ordered magnetic structure while martensite has a disordered magnetic structure, ΔS_{mag} is decreased during the process of magnetic-field induced inverse martensitic transformation. Clearly, the sign of ΔS_{mag} is opposite to ΔS_{vib} and ΔS_{tr}. Thus, in the NiMnIn-based alloy, ΔS_{mag} plays a negative contribution to ΔS_{tr}. For the contribution of electronic structure change on ΔS_{tr}, since both austenite and martensite exhibit the conductivity of metal in the reported NiMnIn alloys, ΔS_{elec} usually makes a negligible contribution to ΔS_{tr}. For example, ΔS_{tr} of the $Ni_{45}Co_5Mn_{36.5}In_{13.5}$ alloy was determined to be ~23 J kg^{-1} K^{-1}, where ΔS_{vib}, ΔS_{mag}, and ΔS_{elec} were about 51, −29, and 1.2 J kg^{-1} K^{-1}, respectively (Kihara et al., 2014). From the above analyses, under the condition of constant ΔS_{vib}, decreasing the negative contribution of ΔS_{mag} should be the most effective method to improve ΔS_{tr} and then ΔS_M (or ΔT_{ad}).

Intuitively, the most direct way to decrease the negative contribution of ΔS_{mag} is to reduce the magnetization difference between austenite and martensite ΔM. However, as discussed in the first half of this section, a remarkable ΔM, directly related to the Zeeman energy ($\mu_0 H\Delta M$), is the prerequisite of the occurrence of magnetic-field induced martensitic transformation. Therefore, from the perspective of the MCE performance, a moderate ΔM is appropriate. In experiments, the most utilized strategy to reduce ΔS_{mag} is to reduce the temperature distance between the magnetostructural transition T_M and the Curie temperature of austenite T_C^A, i.e., $T_C^A - T_M$. Specifically, this is achieved by elevating T_M to make it approach T_C^A. During this process, on the one hand, the magnetization difference between austenite and martensite ΔM is decreased, and then the negative contribution of ΔS_{mag} is weakened. On the other hand, ΔM still possesses a relatively large value since T_M is still lower than T_C^A, which guarantees a remarkable Zeeman energy to ensure the occurrence of the magnetic field-induced reverse martensitic transformation. Thus, one of the key issues of weakening ΔS_{mag} is to adjust T_M.

Different from mechanical properties that are strongly dependent on microstructure, T_M belongs to the inherent property of materials and thus is mainly determined by the chemical composition. Aimed at reducing ΔS_{mag} by tailoring T_M, for the ternary NiMnIn alloys, several alloying methods including changing relative contents of different elements of the alloy and adding the fourth alien elements, such as Cu (Li et al., 2019a; Yan et al., 2021a; Huang et al., 2021), Cr (Sharma et al., 2010a; Sharma et al., 2011), Fe (Chen et al., 2012; Feng et al., 2012), Ga (Paramanik and Das, 2016) and Pd (Li et al., 2015), have been utilized. For instance, under the guidance of valence electron concentration (e/a) criteria of T_M, i.e., a larger e/a corresponds to a higher T_M (Wei et al., 2016), Feng et al. elevated T_M of $Ni_{50}Mn_{34}In_{16}$ from 250 K to 303 K *via* the partial substitution of a low valence electron number (VEN) element of In ($5s^2p^1$, VEN = 3) by a high VEN element of Fe ($3d^64s^2$, VEN = 8) (Feng et al., 2012). In the Fe-doped $Ni_{50}Mn_{34}In_{14}Fe_2$ alloy, T_M almost coincides with T_C^A, and a ΔS_M of 53.6 J kg^{-1} K^{-1} was realized under an 8 T magnetic field at 303 K. In addition, under the guidance of lattice volume effect of T_M, i.e., a contracted lattice tends to elevate T_M (Paramanik and Das, 2016), Sharma et al. shifted T_M of $Ni_{50}Mn_{34}In_{16}$ to a higher temperature (Sharma et al., 2010b). In the $Ni_{50}Mn_{33.66}Cr_{0.34}In_{16}$ alloy, a ΔS_M of 17.7 J kg^{-1} K^{-1} was obtained under a magnetic field of 8T at 270 K.

For the Co-doped NiCoMnIn alloys, compared with ternary NiMnIn alloys, the negative contribution of ΔS_{mag} to ΔS_{tr} is more pronounced as the addition of Co greatly enhances the magnetism of austenite and then the value of ΔM (Li et al., 2019a; Yang et al., 2020). The strategy of weakening ΔS_{mag} in the NiCoMnIn alloy is the same as that of NiMnIn, i.e., elevating T_M to make it close to T_C^A by doping a fifth alien element, such as Cu (Li et al., 2019b; Yan et al., 2021a; Huang et al., 2021), Fe (Chen et al., 2012), Ga (Paramanik and Das, 2016), Pd (Li et al., 2015). With respect to the ternary NiMnIn alloys, in these cases, two elements, i.e., Co and a fifth element, are doped. Thus, this alloying method was sometimes termed as co-doping (Li et al., 2019c). Compared with doping with a single element, the improvement of the MCE performance by the co-doping is usually more prominent. For instance, by co-doping with Co and Cu, Z. B. Li and collaborators realized a large ΔT_{ad} up to −4.8 K under a low-field change of 1.5 T in the $Ni_{46}Co_3Mn_{35}Cu_2In_{14}$ alloy at 272 K (Li et al., 2019a).

c) Utilizing multicaloric effect. As discussed above, the incompleteness of magnetic field-induced inverse martensitic transformation due to the high critical magnetic field required for a full transformation is a critical issue that restricts the MCE performance of the NiMnIn-based alloys.

Inspired by the fact that apart from the magnetic field, the martensitic transformation of NiMnIn alloy can also be triggered by mechanical field, an idea of improving MCE by simultaneously or sequentially applying mechanical and magnetic fields was proposed. Owing to the existence of multiple stimuli, the caloric effect generated in this process is termed as the multicaloric effect (Stern-Taulats et al., 2018). Compared with the caloric response when subjected to a single stimulus, the multicaloric effect generally has a much higher refrigeration capacity (Gràcia-Condal et al., 2020). In the $Ni_{50}Mn_{35.5}In_{14.5}$ alloy, by applying a magnetic field of 4 T and a mechanical field of 40 MPa, a multicaloric effect with an entropy change of 25.2 $J\,kg^{-1}\,K^{-1}$ and an adiabatic temperature change of 5.9 K was realized at room temperature. These values obviously exceed that of single magnetocaloric and elastocaloric effects.

6.2 Thermal/Magnetism Hysteresis

In application, to realize a real MCE refrigeration, the magnetic field needs to be repeatedly applied to the MCE refrigerant (around 10^7 times), which requires that the MCE effect possess a good cyclability. Unfortunately, different from MCE around the second-order Curie transition, MCE originated from the first-order magnetostructural transition is inevitably accompanied with the transitional thermal hysteresis ΔT_{Hys}. Theoretically, ΔT_{Hys} caused by the energy barrier between austenite and martensite is closely related to the transitional stress layer between the two phases. During the cyclic transformation, the stress in the transitional layer could induce certain irreversible processes, such as the formation of dislocations and the nucleation of microcracks, which further lead to functional degradation and failure (Song et al., 2013). Thus, for the practical applications, it is greatly meaningful to reduce ΔT_{Hys} and improve the reversibility of magnetostructural transition of the NiMnIn alloys. Until now, several strategies have been proposed, aimed at reducing ΔT_{Hys}, such as improving geometric compatibility between austenite and martensite, applying extra stimuli, etc.

a) Enhancing geometrical compatibility between austenite and martensite: As mentioned above, the degradation of cyclability is associated with the transitional stress layer between austenite and martensite. Thus, reducing the transition layer will be able to fundamentally decrease ΔT_{Hys} and improve the functional stability. According to the crystallographic theory of martensitic transformation (Nishiyama, 1978; Christian, 2002), the transitional stress layer is closely related to the geometrical compatibility between austenite and martensite, which can be described quantitatively by the middle eigenvalue of transformation stretch tensor λ_2 and the more strict cofactor condition (Chen et al., 2013; Song et al., 2013; Della Porta, 2019). A thinner transitional layer corresponds to better geometrical compatibility. For the geometrical compatibility between austenite and martensite, it is purely determined by the lattice parameters of these two phases, which can be adjusted by tailoring the chemical composition of the alloy. This provides an effective method to reduce ΔT_{Hys}.

For the ternary NiMnIn alloys, it is reported that the substitution of Cu for Mn is a valid method to improve the geometrical compatibility and thus decreases ΔT_{Hys} (Zhao et al., 2017a). For instance, D. W. Zhao et al. achieved a small ΔT_{Hys} of 3K and an excellent phase transition stability over 10^5 magnetic field cycles in the Cu-doped $Ni_{50}Mn_{31.5}In_{16}Cu_{2.5}$ alloy (Zhao et al., 2017b). They attributed the low ΔT_{Hys} and the exceptional cyclic stability to the fact that in this compound, λ_2 (0.99281) is fairly close to 1 and the (011) type-I/II twins, together with the (100) compound twins, closely satisfy the co-factor conditions simultaneously (Zhao et al., 2017a).

For the NiCoMnIn alloys, even though the addition of Co can enhance the magnetism of austenite and further significantly improve the magnetoresponsive behaviors, unfortunately, this alloying leads to a significant increase in hysteresis and phase transition irreversibility. For example, ΔT_{hys} of the ternary NiMnIn alloys is around 5–12 K, while with the addition of Co the value of ΔT_{hys} abruptly elevates to 10–30 K (Yan et al., 2021a). Thus, for the NiCoMnIn alloys, the harm caused by the thermal hysteresis and the irreversibility of phase transition is more severe compared with that in the ternary NiMnIn alloys. Until now, apart from Co, several fifth alloying elements were co-added to the NiMnIn alloys aimed at optimizing the hysteresis behavior, such as Co & Fe (Chen et al., 2012), Co & Si (Li et al., 2019b), Co & Cu (Li et al., 2019c; Yan et al., 2021b; Huang et al., 2021). Z. B. Li et al. reported that the Cu substitution for Mn can effectively reduce ΔT_{Hys} of the NiCoMnIn alloys from 17.5 K ($Ni_{46}Co_3Mn_{36}Cu_1In_{14}$) to 9 K ($Ni_{46}Co_3Mn_{34}Cu_3In_{14}$) (Li et al., 2019a). In the Co and Cu co-doped $Ni_{46}Co_3Mn_{35}Cu_2In_{14}$ alloy, they achieved a reversible ΔS_M of 16.4 $J\,kg^{-1}\,K^{-1}$ under a magnetic field of 5 T and a reversible ΔT_{ad} of 2.5 K under a magnetic field of 1.5 T (Li et al., 2019b).

Nevertheless, this alloying strategy of Cu, i.e., replacing Mn, will inevitably lead to the reduction of magnetism, since the magnetic moment of the Ni–Mn-based alloys is mainly provided by Mn (~85%) (Yan et al., 2020a; Yan et al., 2020b). To avoid the negative influence on magnetism caused by Cu doping, the co-alloying strategy with Cu replacing In and Co replacing Mn was studied (Yan et al., 2021a). In the $Ni_{45}Co_5Mn_{36}In_{13.3}Cu_{0.7}$ alloy, a reversible isothermal magnetic entropy change of 13.8 $J\,kg^{-1}\,K^{-1}$ and a refrigeration capacity of 270.2 $J\,kg^{-1}$ were obtained. Moreover, when the geometrical compatibility between austenite and martensite is improved by adjusting lattice parameters via tailoring the chemical composition, the volume variation ratio $\Delta V/V_0$ during the transition that is closely related to the transformation entropy change will inevitably be changed. The alloying strategy of improving geometrical compatibility and keeping remarkable $\Delta V/V_0$ meanwhile is still an open issue.

b) Applying extra stimulus fields: For the NiMnIn based alloys, owing to the strong coupling between magnetism and crystal lattice, the magnetostructural transformation is sensitive to both magnetic field and stress/strain field. This provides another way to tailor the hysteresis behavior of MCE, i.e., the stress/strain-assisted transformation. J. Liu et al. reported that the application of bias stress can greatly reduce or even eliminate the magnetic hysteresis during the

cycle of the magnetic field-induced inverse martensitic transformation (Liu et al., 2012; Zhao et al., 2017a). They observed that if the sample is magnetized without bias stress but is demagnetized under a low external hydrostatic pressure of 1.3 kbar, the isothermal magnetization and demagnetization curves of the NiCoMnIn alloy almost coincide (Liu et al., 2012).

By utilizing the bias stress, T. Gottschall et al. proposed a multicaloric cooling cycle to eliminate the negative influence of hysteresis on the reversibility of phase transition (Gottschall et al., 2018). The key idea of this method is to apply uniaxial stress to assist the transformation of the ferromagnetic austenite phase locked by large hysteresis into the martensite phase. The caloric effect is expected to be reproducible under the following sequence: 1) a decrease in temperature when the NiMnIn-based alloys are adiabatically magnetized; 2) the reverse transition does not happen due to the existence of thermal hysteresis during demagnetization; 3) absorbing heat from surroundings in the absence of a magnetic field; 4) applying uniaxial stress to assist the transformation from austenite to martensite; 5) removing stress; 6) expelling heat to the surroundings. By alternately applying a magnetic field (1.8T) and a stress field (80 MPa), they obtained a reversible ΔT_{ad} of −1.2 K in the $Ni_{49.6}Mn_{35.6}In_{14.8}$ alloy (Gottschall et al., 2018).

Apart from bias stress, Z. Z. Li et al. reported that the existence of the internal stress introduced by the pre-deformation can also improve the MCE cyclability (Li et al., 2018). They found that by applying pre-deformation, the reversible ΔT_{ad} of the $Ni_{45.3}Co_{5.1}Mn_{36.1}In_{13.5}$ alloy increases to 1.1 K from 0.8 K (the stress-free state). Besides, Y.-Y. Gong et al. reported that the strain-assisted transformation can also effectively tailor the hysteresis behavior of the NiCoMnIn alloy (Gong et al., 2015). They found that the strain generated by the PMN-PT piezoelectric ceramics can decrease ΔT_{Hys} from 25.5 to 21.6 K with an electric field varying from 0 to 8 kV cm^{-1}.

c) Other methods: Apart from tailoring geometrical compatibility and applying external stress/strain stimuli, the microstructure of MCE refrigerant was also reported to have an important influence on hysteresis. J. Liu et al. found that for the $Ni_{45}Mn_{37}In_{13}Co_5$ ribbons sample, the annealing can reduce the thermal hysteresis from 25 K to 20 K (Liu et al., 2009b). They attributed the reduction of ΔT_{ad} to the increased grain size and decreased defect density. Besides, T. Gottschall et al. proposed that the transformation performed in a minor loop instead of a complete transformation can improve the MCE stability (Gottschall et al., 2015). With this method, they obtained a cyclic ΔT_{ad} of −3 K at the magnetic field of 1.95 T in the $Ni_{45.7}Mn_{36.6}In_{13.5}Co_{4.2}$ alloy (Gottschall et al., 2015).

6.3 Working Temperature Window

For the NiMnIn-based alloys, different from the conventional giant MCE which occurs around the second-order Curie transition, the excellent MCE in these compounds is originated from the first-order magnetostructural transition. During the second-order Curie transition, the order parameter, i.e., magnetization, experiences a continuous transition in a relatively wide temperature change (40–50 K). In contrast, the first-order martensitic transformation occurs in a burst manner at speed close to that of the sound. The difference in the transformation speed of the first-order and the second-order phase transition results in a large difference in the operating temperature window of the corresponding MCE. An example comparing the MCE operating temperature window widths of the first-order and second-order transitions is illustrated in **Figure 10**. It is seen that the operating temperature range δT_{FWHM} defined as the full width at half maximum of $\Delta S_M(T)$ curve of Gd (second-order Curie transition) is around 47 K, which is about 6 times wider than that of $Gd_5Si_2Ge_2$ (first-order magnetostructural transition) (Pecharsky and Gschneidner, 1997). For the MCE, the refrigeration capacity (RC) is determined by the product of isothermal magnetic entropy change ΔS_M and the operating temperature window δT_{FWHM}. Thus, a narrow δT_{FWHM} will lead to a significant reduction in refrigeration capacity. So far, numerous strategies have been proposed to expand the operating temperature window of the MCE, such as enhancing the magnetic field sensitivity of magnetostructural transition temperature T_M, preparing composite material containing the MCE refrigerants with different T_M, and combining different caloric responses (magnetocaloric and elastocaloric).

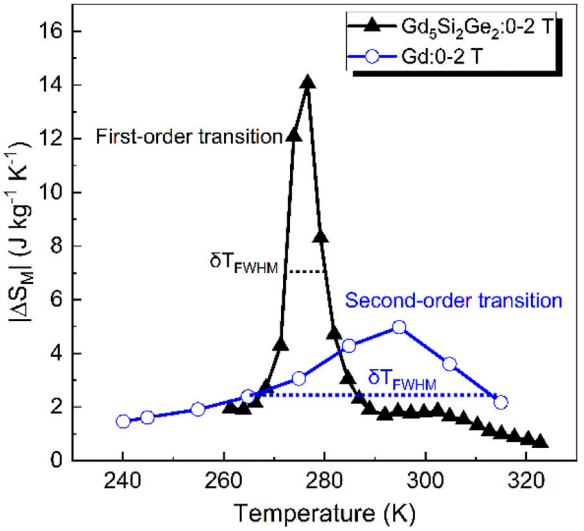

FIGURE 10 | Isothermal magnetic entropy change of the $Gd_5Si_2Ge_2$ between 240 and 325 K for a magnetic field change from 0 to 2 T, compared with that of pure Gd as determined from magnetization measurement (Pecharsky and Gschneidner Jr., 1997).

a) Enhancing the magnetic field sensitivity of magnetostructural transition temperature $\Delta T/\Delta H$: Fundamentally, for the MCE associated with the first-order magnetostructural transition, the width of the operating temperature window is decided by the magnetic field sensitivity of magnetostructural transition temperature $\Delta T/\Delta H$. Under a certain magnetic field, a higher $\Delta T/\Delta H$ value will lead to a larger shift of magnetostructural

transition temperature, further resulting in a wider operating temperature window δT_{FWHM}. Based on the Clausius-Clapeyron equation, as discussed previously, the $\Delta T/\Delta H$ value can be increased by enlarging the magnetization difference between austenite and martensite ΔM, which can be achieved by the partial substitution of Co for Ni. For instance, by introducing Co, the value of δT_{FWHM} increases from 24 K ($Mn_{50}Ni_{39}In_9Co_2$) to 32 K ($Mn_{50}Ni_{37}In_9Co_4$) (Yang et al., 2020). However, as mentioned earlier, the substitution of Co will increase ΔT_{hys}. To weaken the negative effect on ΔT_{hys}, L. M. Wang proposed a low content of Co alloying method aiming at simultaneously realizing a wide $\Delta T/\Delta H$ and low ΔT_{hys} (Wang et al., 2020). In the $Ni_{48}Co_1Mn_{37}In_{14}$ alloy, a working temperature range of 34 K and an effective refrigeration capacity of 284 J kg^{-1} were realized under a magnetic field of 5 T.

b) Combining different caloric responses: For the NiMnIn-based alloys, apart from the inverse MCE associated with the first-order magnetostructural transition, it also exhibits the elastocaloric effect (see details in **Section 7**) and the conventional MCE around the second-order Curie transition of austenite. As is known, the magnetic field tends to stabilize the phase with strong magnetism, i.e., austenite, while the mechanical field stabilizes martensite preferentially. Therefore, the transitional temperature of martensitic transformation T_M tends to shift towards an opposite direction when the magnetic field and the stress field are applied, respectively. As a result, although both inverse MCE and elastocaloric effects are associated with martensitic transformation, typically, the working temperature ranges for the inverse MCE and the elastocaloric effect are, respectively, lower and higher than T_M. This characteristic of the NiMnIn-based alloys provides a novel route to widen the working temperature range, i.e., combining the different caloric responses with adjacent temperature ranges. Moreover, by composition design, MCE associated with the second-order Curie temperature can also be adjusted near the magnetostructural transition. In this situation, the inverse MCE, the elastocaloric effect, and the conventional MCE can be combined and further expand the refrigeration temperature region.

In 2017, Y. Hu et al. proposed the method of widening the operating temperature window by combining elastocaloric and MCE effects. By using this method, they realized a broad refrigeration temperature region of around 120 K in the $Ni_{49.5}Mn_{28}Ga_{22.5}$ alloy (Hu et al., 2017). In the $Ni_{50}Mn_{35}In_{15}$ alloy, Z. B. Li et al. realized a broad refrigeration temperature region ranging from 270 K to 380 K *via* the combination of successive MCE and elastocaloric effects (Li et al., 2020). Recently, P. T. Cheng et al. realized a refrigeration temperature range of 250–340 K in the $Ni_{45}Co_5Mn_{37}In_{13}$ alloy by using the same strategy (Cheng et al., 2021).

c) Utilizing the intermediate martensitic transformation: In some NiMnIn-based alloys, an intermediate martensitic transformation has been observed, i.e., the martensitic transformation occurs in multiple stages. By using the multi-stage phase transition characteristics, the operating temperature window of MCE can be extended if different stages of martensite transformation occur in an adjacent temperature range. For example, S. Dwevedi et al. reported a two-step martensitic transformation in the Sn-doped Ni–Mn–In-based alloys, which leads to the double peak behavior of ΔS_M and widens the operating temperature range (Dwevedi and Tiwari, 2012). With a two-step martensitic transformation, an operating temperature window δT_{FWHM} of around 46.5 K was realized in the $Ni_{50}Mn_{34}In_8Sn_8$ alloy that greatly exceeds the typical δT_{FWHM} value of the single-stage martensitic transformation (~10 K at a magnetic field of 2 T).

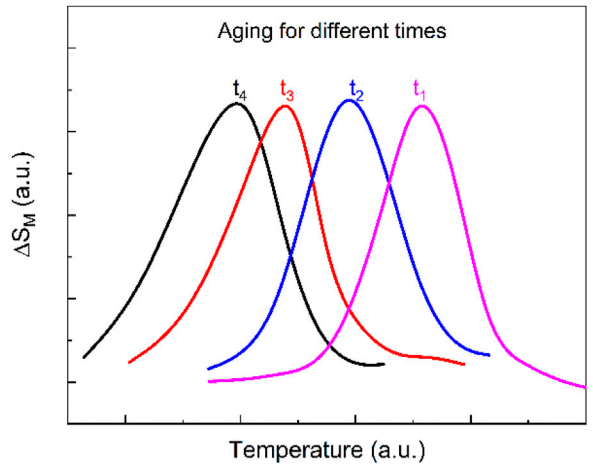

FIGURE 11 | Realizing a wide operating temperature window by combining various samples with different aging times.

d) Fabricating composite material containing the MCE refrigerants with different T_M: For the MCE associated with the first-order magnetostructural transition, the operating temperature is around the temperature of magnetostructural transition. Thus, fabricating a series of MCE refrigerants with different T_M and compositing them will allow to greatly expand the operating temperature range. Using this strategy, J. Liu et al. proposed a method of stacking a series of alloys with different annealing times to successfully expand the operating temperature window of the NiCoMnIn alloy(Liu et al., 2012). For the NiCoMnIn alloys, with the prolongation of aging time, the martensitic transformation is gradually shifted to the lower temperatures, whereas the transformation entropy change remains unchanged. Thus, for the composite containing a series of alloys aged at different times, the operating temperature window is greatly enlarged, as illustrated in **Figure 11**. Later, J.-P. Camarillo et al. reported that a reversible ΔS_M of 7.5 J kg^{-1} K^{-1} was obtained over a broad temperature range of 30 K by assembling a composite specimen in a NiMnInCu alloy (Camarillo et al., 2016).

6.4 Perspectives

From the above discussion, the high magnetic moment of austenite, which usually brings about a large magnetization difference ΔM between austenite and martensite, is a double-edged sword for the MCE performance. On the one hand, a remarkable ΔM is a prerequisite for the magnetic field-induced inverse martensitic transformation. On the other hand, a higher ΔM makes a larger negative contribution of ΔS_{mag} to ΔS_{tr}. Thus, for the optimized MCE performance, ΔM should be neither too big nor too small. For the multicaloric effect, it is indeed possible to improve refrigeration efficiency. Unfortunately, compared with the single stimulus, the multiple stimuli significantly increase the complexity of machine construction and equipment cost. More efforts focused on optimizing the structure of the equipment are required. Apart from the above-mentioned strategies, in our opinion, the methods of improving lattice vibration entropy change ΔS_{vib} and electronic entropy change ΔS_{elec} may open new ways to improve the MCE performance. Since ΔS_{tr} is mainly decided by ΔS_{vib}, the method of enlarging ΔS_{vib} could greatly improve the MCE performance. In addition, even though in the known NiMnIn-based alloys, ΔS_{elec} plays a negligible positive role on ΔS_{tr}, it might be possible to obtain a large ΔS_{elec} by tailoring the electronic structure of martensite from metal to semiconductor state. The semiconducting state is not uncommon in the 2:1:1 type Heusler alloys. Recently, J. C. Lin et al. found that ΔS_{elec} plays a key role on ΔS_{tr} in the $Ni_{1-x}Fe_xS$ alloy during the study of barocaloric effect (Lin et al., 2020), which evidenced that it is feasible to utilize ΔS_{elec} to improve ΔS_{tr}.

Through the above-mentioned strategies, the thermal/magnetic hysteresis of the Ni(Co)MnIn alloys has been greatly optimized. However, the cyclic stability of the MCE performance of the Ni(Co)MnIn alloys yet cannot meet the needs for practical applications. For instance, in the state-of-the-art Co and Cu co-doped $Ni_{46}Co_3Mn_{35}Cu_2In_{14}$ alloy, the maximum ΔT_{ad} is up to −4.8 K under the magnetic field of 1.5 T at the first cycle, while this value rapidly drops to −2.5 K at the second cycle (Li et al., 2019c). So far, there is still a lack of satisfactory alloying methods, which can substantially improve the geometrical compatibility of the alloy without degrading other parameters required for MCE. One of the difficulties is that the geometrical compatibility rule is a posteriori criterion. Specifically, the geometrical compatibility factors can only be calculated with the measured lattice parameters of austenite and martensite after the alloy is fabricated. This method is inefficient and cannot be directly used to guide the design of alloy composition. So far, the direct relation between alloy composition and geometrical compatibility is unknown. High throughput experimental or computational methods and machine learning may provide a feasible way to find the correlation and then promote the design of low-hysteresis NiMnIn alloys.

7 ELASTOCALORIC EFFECT

Elastocaloric effect (eCE) refers to the caloric response of material when external uniaxial stress is applied (Brown, 1981). Compared with the MEC and the electrocaloric effect, the elastocaloric effect is of high work efficiency, environmental friendliness, and low cost. Therefore, the elastocaloric refrigeration technique has been considered to be the most promising alternative to replace traditional vapor compression technology for room-temperature refrigeration (Goetzler et al., 2014), such as air conditioners and fridges. Besides, owing to the convenience of mechanical loading, the elastocaloric effect also exhibits promising potential application in the field of micro- or nano-refrigeration, such as the microelectronic chip. In recent years, some significant progress has been made in the design and development of elastocaloric refrigeration devices (Schmidt et al., 2015; Tušek et al., 2016; Kabirifar et al., 2019).

At present, the discovered elastocaloric material includes natural rubber, shape memory alloy, ion or molecular compound, and rare-earth-based compound. Among them, the shape memory alloy possesses a remarkable refrigeration capacity with the adiabatic temperature change of 3–30 K (Mañosa et al., 2010; Lu et al., 2014; Moya et al., 2014; Liu et al., 2017; Manosa and Planes, 2017; Kabirifar et al., 2019), which is much larger than those of ion or molecular compounds and rare earth compounds, such as 0.42 K for $Ce_{0.85}(La_{0.95}Y_{0.05})_{0.15}Sb$ and 0.4 K for HoAs (Nikitin, 2011; Cazorla, 2019; Zhang et al., 2020). Moreover, the constituent elements of shape memory alloy are relatively abundant and cheap compared with the rare-earth-based compounds. Among numerous shape memory alloys, NiMnIn-based magnetic shape memory alloys represent a special category owing to the relatively low critical driving stress (100–300 MPa) (Lu et al., 2014; Huang et al., 2019; Li et al., 2020).

For shape memory alloy materials, the large elastocaloric effect is originated from the process of stress-induced martensitic transformation. During the loading-unloading cycle, the release and the absorption of the latent heat are used to achieve refrigeration, as illustrated in **Figure 12**. When uniaxial stress is applied to austenite, at the condition that the applied stress exceeds the critical stress to drive martensitic transformation σ_M^S, the alloy will transform from a high-temperature austenite phase to a low-temperature martensite phase (stage ② in **Figure 12A**). During this process, the latent heat of phase transition will be released, leading to a rise in the temperature of the refrigerant (stage ② in **Figure 12B**). When the load is removed, the sample experiences a process of inverse martensitic transformation and returns to the austenitic state (stage ⑥ in **Figure 12A**). In the process, the refrigerant absorbs heat from the environment, leading to a decrease in the temperature of the sample (stage ⑥ in **Figure 12B**).

Like MCE, eCE is characterized by the isothermal entropy change ΔS_{iso} and adiabatic temperature change ΔT_{ad}. For the NiMnIn alloys, eCE was first reported by Lu et al. (2014). In the textured $Ni_{45.7}Mn_{36.6}In_{13.3}Co_{5.1}$ polycrystalline sample, they observed a reversible ΔT_{ad} of 3.5 K under uniaxial stress of 100 MPa at room temperature. Later, Y. J. Huang et al. realized a ΔT_{ad} of −4 K in the ternary $Ni_{48}Mn_{35}In_{17}$ directionally solidified alloy (Huang et al., 2015). Among various known eCE refrigerants, the required critical stress for martensitic transformation σ_M^S is relatively small (~100 MPa) in

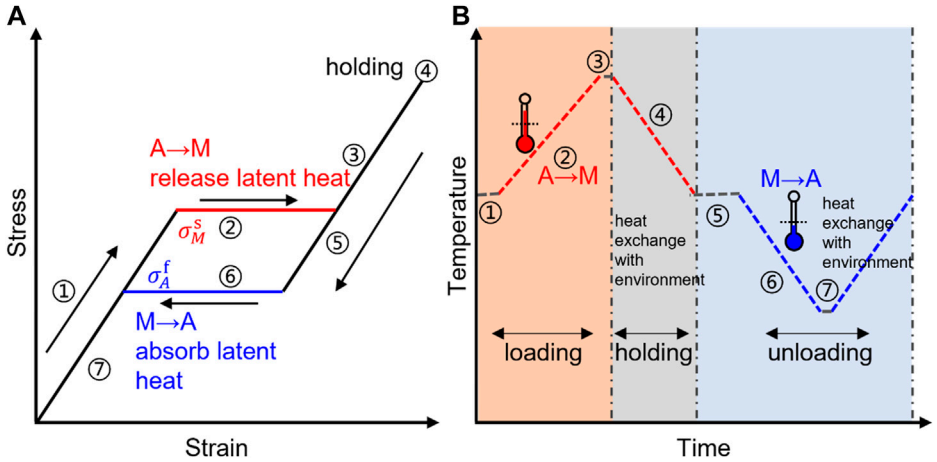

FIGURE 12 | Schematic diagram of **(A)** stress-strain curve and **(B)** corresponding temperature change for eCE of shape memory alloys. The temperature variations of ① to ⑦ in **(B)** exactly correspond to the stages of ① to ⑦ in the stress-strain curve of **(A)**.

TABLE 2 | Research progress of elastocaloric effect in the NiMnIn-based alloys.

Year	Reference	Alloy composition (at%)	Sample state	eCE			Stress	Test temperature
				ΔS_{iso} J kg^{-1} K^{-1}	ΔT K	COP	MPa	K
2014	Lu et al. (2014)	$Ni_{45.7}Mn_{36.6}In_{13.3}Co_{5.1}$	Oriented polycrystalline		−3.5		100	300
2015	Huang et al. (2015)	$Ni_{48}Mn_{35}In_{17}$	Oriented polycrystalline	10.3	−4		300	313.3
2015	Lu et al. (2015)	$Ni_{45}Mn_{36.4}In_{13.6}Co_5$	Bulk Polycrystalline		−4		150	296
2016	Shen et al. (2017)	$Ni_{51.4}Mn_{34}In_{15.6}Tb_{0.4}$	Bulk Polycrystalline		−5.1		622	291
2017	Zhao et al. (2017b)	$Ni_{45}Mn_{36.5}In_{13.5}Co_5$	Oriented polycrystalline		+8.6		260	298
2017	Lu and Liu (2017)	$Ni_{45}Mn_{36.4}In_{13.6}Co_5$	Bulk Polycrystalline		−3		135	293
		$Ni_{45}Mn_{36}In_{14}Co_5$			−2		340	287
		$Ni_{45}Mn_{36.2}In_{13.8}Co_5$			−3.1		225	room temperature
2017	Yang et al. (2017)	$(Ni_{51.5}Mn_{33}In_{15.5})_{99.7}B_{0.3}$	Bulk Polycrystalline	20	−6.2	18	550	303
2017	Zhao et al. (2017a)	$Ni_{50}Mn_{31.5}In_{16}Cu_{2.5}$	Oriented polycrystalline	−23.1	+13		280	room temperature
2017	Camarillo et al. (2017)	$Ni_{51.4}Mn_{33.6}In_{12.1}Ga_{2.9}$	Bulk Polycrystalline	25	−4.9		100	room temperature
2018	Henández-Navarro et al. (2018)	$Ni_{50}Mn_{32}In_{16}Cr_2$	Bulk Polycrystalline		−3.9		100	room temperature
2018	Shen et al. (2018)	$Ni_{45}Mn_{36}In_{13}Co_5Cr$	Bulk Polycrystalline		−5.8		300	323
2019	Huang et al. (2019)	$Ni_{50}Mn_{34.8}In_{15.2}$	Oriented polycrystalline	–	−7.6	–	345	room temperature
2019	Tang et al. (2019)	$(Ni_{52}Mn_{31}In_{16}Cu_1)B_{0.2}$	Bulk Polycrystalline		−9.5		220	room temperature
2019	Yang et al. (2019)	$(Ni_{51}Mn_{33}In_{14}Fe_2)_{99.4}B_{0.6}$	Bulk Polycrystalline		+5.6		350	304
2019	Li et al. (2019c)	$Ni_{44.9}Co_{4.9}Mn_{36.9}In_{13.3}$	Oriented polycrystalline		+14.7		650	390
2020	Huang et al. (2020)	$Ni_{50}(Mn_{31.7}Cu_{2.5}B_{0.3})In_{15.5}$	Oriented polycrystalline	–	−12.8	–	500	room temperature
2020	Li et al. (2020)	$Ni_{50}Mn_{35}In_{15}$	Oriented polycrystalline		−19.7		350	320
2021	Cheng et al. (2021)	$Ni_{45}Co_5Mn_{37}In_{13}$	Oriented polycrystalline	10	−6		200	303

the NiMnIn-based alloys (Lu et al., 2014; Huang et al., 2019; Cheng et al., 2021), which makes this kind of compounds have broad prospects in the fields of micro- and nano-refrigeration, such as microelectronic chips. From then on, the eCE of the NiMnIn-based alloys has been attracting more and more attention. Some representative work associated with eCE of the NiMnIn-based alloys are summarized in **Table 2**.

Until now, the studies on the eCE of the NiMnIn-based alloys were mainly focused on the following two aspects: 1) elevating adiabatic temperature change ΔT_{ad} that is directly linked to the refrigeration capacity. A large ΔT_{ad} is a constant pursuit to improve the energy conversion efficiency; 2) improving mechanical properties. Different from the MCE, the eCE has a much higher requirement on the mechanical properties of a refrigerant since the refrigeration material must bear a large mechanical load during work. Unfortunately, owing to the strong covalent *p-d* hybridization between the *p* valence electrons of the *p-block* element of In and the *3d* valence electrons of Ni (and Mn) (Bechtold et al., 2012; Qian et al., 2015; Liu et al., 2017), the NiMnIn-based alloys are intrinsically brittle, which will introduce structural fatigue and do harm to cyclic stability of eCE. Next, the main progress related to these two aspects of the Ni–Mn–In-based alloys will be briefly reviewed.

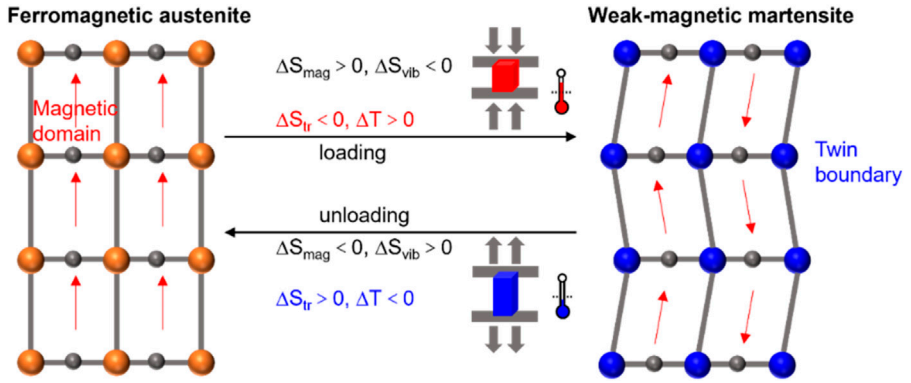

FIGURE 13 | Schematic diagram of the entropy change of magnetostructural transition in NiMnIn-based alloys.

7.1 Adiabatic Temperature Change

Like the isothermal magnetic entropy change ΔS_M of the MCE, the upper limit of isothermal entropy change ΔS_{iso} (or adiabatic temperature change ΔT_{ad}) of eCE is determined by the transformation entropy change ΔS_{tr}. As discussed in **Section 6**, for the NiMnIn-based alloys, the sign of magnetic entropy change ΔS_{mag} is opposite to the total transformation entropy change ΔS_{tr} (**Figure 13**). Therefore, one of the critical issues of increasing ΔS_{tr} is to reduce the negative contribution of magnetic entropy change ΔS_{mag}. To optimize the eCE of the NiMnIn-based alloys by means of weakening ΔS_{mag}, as illustrated in **Figure 14**, several methods have been proposed, including (a) elevating the temperature of magnetostructural transition T_M to make it close (or above) the Curie temperature of austenite, (b) increasing the testing temperature T_{Test} to make it close (or above) the Curie temperature of austenite, and (c) reducing the magnetism of austenite.

a) Elevating the temperature of magnetostructural transition T_M to (or above) the Curie temperature of austenite: As utilized in improving the MCE performance, as illustrated in **Figure 14A**, ΔT_{ad} of the eCE can also be optimized by elevating the temperature of magnetostructural transition T_M to or above the Curie temperature of austenite to reduce the negative contribution of ΔS_{mag} on ΔS_{tr}. By the partial substitution of Cu for Mn, D. W. Zhao et al. elevated the finish temperature of inverse martensitic transformation (A_f) from 235.0 K of $Ni_{50}Mn_{34}In_{16}$ to 279.8 K of $Ni_{50}Mn_{31.5}In_{16}Cu_{2.5}$. With this substitution, the ΔT_{ad} values of +13 K and −10 K in a directionally solidified $Ni_{50}Mn_{31.5}In_{16}Cu_{2.5}$ sample were obtained during loading and unloading at room temperature, respectively (Zhao et al., 2017b). As can be seen from **Table 2**, this ΔT_{ad} belongs to the relatively high value of room-temperature eCE in the NiMnIn-based alloys. Z. Yang et al. reported that by Fe doping, A_f of 304 K of the $Ni_{51.5}Mn_{33}In_{15.5}$ alloy (e/a = 7.93) is shifted to 319 K in the $Ni_{51}Mn_{33}In_{14}Fe_2$ alloy (e/a = 7.99) (Yang et al., 2019). Under this substitution, ΔT_{ad} was increased from 3 K of $Ni_{51.5}Mn_{33}In_{15.5}$ to 5.7 K of $Ni_{51}Mn_{33}In_{14}Fe_2$ under 350 MPa.

b) Increasing testing temperature T_{Test} to (or above) the Curie temperature of austenite: For the eCE, the temperature at which the structural transition occurs, i.e., the temperature of stress-induced martensitic transformation, is determined by the testing temperature T_{Test}, rather than the temperature of martensitic transformation under zero-field (T_M). Thus, as a conjugate way by T_M, the negative contribution of ΔS_{mag} can be reduced by increasing testing temperature T_{Test} to or above the Curie temperature of austenite, as illustrated in **Figure 14B**. For instance, Z. Z. Li et al. reported that as the test temperature increased from 320 to 390 K under 650 MPa, ΔT_{ad} of the $Ni_{44.9}Co_{4.9}Mn_{36.9}In_{13.3}$ alloy increased from 8.3 to 14.7 K due to the decreased ΔS_{mag} (Li et al., 2019c). Similar to this temperature enhanced eCE, as T_{Test} increased from 310 to 320 K under 350 MPa, ΔT_{ad} of the $Ni_{50}Mn_{35}In_{15}$ alloy increased from −15 to −19.7 K (Li et al., 2020). In addition, as T_{Test} increased from 290 to 314 K under 250 MPa, ΔS_{iso} increased from 15 to 47.8 J kg^{-1} K^{-1} (Li et al., 2020).

c) Reducing the magnetism of austenite: For the MCE performance, as discussed in **Section 6**, the magnetism of austenite is a double-edged sword. On the one hand, a strong magnetism of austenite will lead to a remarkable ΔM and then a large driving force for inverse martensitic transformation; on the other hand, a strong magnetism will bring about a large ΔS_{mag}, which is harmful to the MCE refrigeration capacity. However, for the eCE in which the martensitic transformation is driven by a mechanical field rather than a magnetic field, the magnetism of austenite seems to be a purely harmful factor. Thus, for the eCE performance, the most effective and fundamental method to weaken the negative contribution of ΔS_{mag} is to reduce the magnetism of austenite, as illustrated in **Figure 14C**.

For the Ni–Mn-based alloys, the adiabatic temperature change realized at room temperature is only 3–15 K (Lu et al., 2014; Zhao et al., 2017a; Huang et al., 2020), which is smaller than those of non-magnetic NiTi (10–25 K) (Cui et al., 2012; Pataky et al., 2015; Tušek et al., 2015) and NiMnTi (20–30 K) (Cong et al., 2019; Yan et al., 2019). One of the possible reasons might be associated with

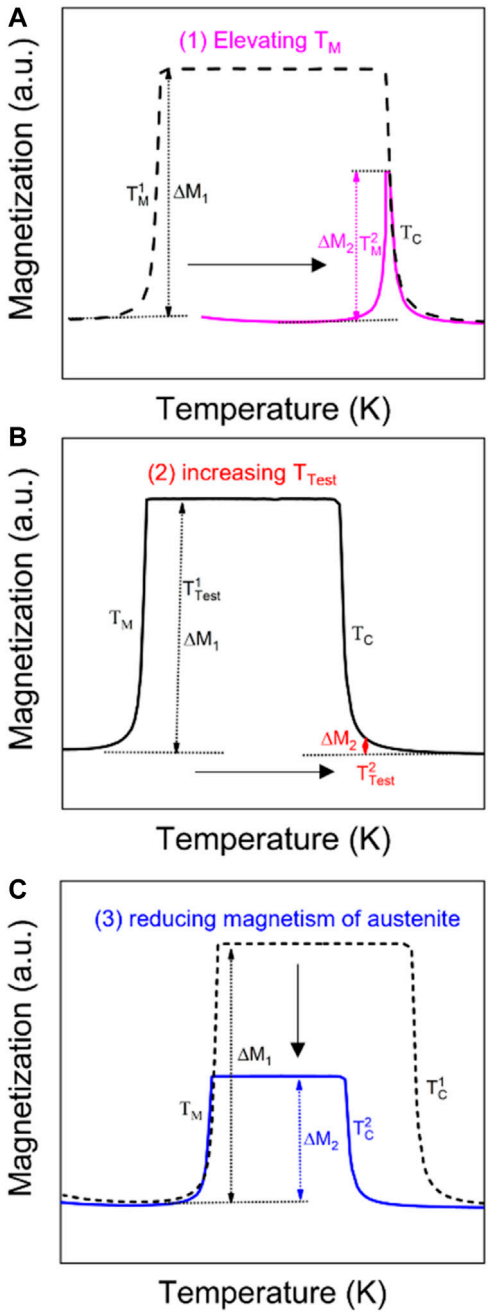

FIGURE 14 | Schematic diagrams of weakening ΔS_{mag} by **(A)** elevating the temperature of magnetostructural transition T_M to make it close (or above) the Curie temperature of austenite, **(B)** increasing the test temperature T_{Test} to make it close (or above) the Curie temperature of austenite, and **(C)** reducing the magnetism of austenite.

the large negative contribution of magnetic entropy change ΔS_{mag}. It is known that the magnetic moment of the Ni–Mn-based alloys is mainly originated from the Mn element. Therefore, decreasing the concentration of Mn, substituted by non-magnetic elements, allows to dramatically reduce the ferromagnetism of austenite and further eliminate the negative contribution of ΔS_{mag}. By using this strategy, with the co-substitution of Cu and B for Mn, X. M. Huang et al. successfully reduced the value of ΔM from 82 to 42 emu g^{-1} and realized a large ΔT_{ad} of −12.8 K in the $Ni_{50}(Mn_{31.7}Cu_{2.5}B_{0.3})In_{15.5}$ directionally solidified alloy (Huang et al., 2020).

7.2 Mechanical Properties and Cyclic Stability

To realize a real application of eCE refrigeration, the number of cyclic loading-unloading around 10^7 times (Chluba et al., 2015) of uniaxial stress to the eCE refrigerant is necessary, which requires that the eCE refrigerant be mechanically stable. As discussed above, the NiMnIn-based alloys are intrinsically brittle due to the high covalency in chemical bonds, which greatly reduces the fatigue fracture resistance of the material and thus is detrimental to the cyclic stability of the eCE. Aimed at improving the mechanical properties of the NiMnIn-based alloys, several methods have been proposed to enhance the mechanical properties, such as grain refinement (Yang et al., 2017; Yang et al., 2019; Huang et al., 2020), grain boundary strengthening (Huang et al., 2015; Zhao et al., 2017b; Huang et al., 2019), introducing coarse columnar crystals with strong texture (Huang et al., 2015; Zhao et al., 2017a; Huang et al., 2019), and introducing a soft second-phase (Yang et al., 2015; Shen et al., 2018).

a) Grain refinement: For the NiMnIn-based polycrystalline alloys, since the transformation strain ε_{trans} is strongly orientation-dependent (**Section 4.2**), the strain discontinuity would inevitably occur near the grain boundary of the austenite with different orientations, especially at triple junctions. Thus, cracks may nucleate at the grain boundaries of austenite and propagate along the grain boundaries due to the relative weakness of the grain boundary with respect to the grain interior in intermetallics. For the refined samples, the reduced grain size leads to the decrease of the difference of cumulative transformation displacements $d{\cdot}\varepsilon trans$ between two austenite grains. Thus, the nucleation and the propagation of the crack might be suppressed. As a result, the strength and toughness of the material will be improved.

V. Sánchez-Alarcos et al. reported that the Ti doping can refine the grain size from 1160 μm ($Ni_{50}Mn_{33.5}In_{16.5}$) to 40 μm [$(Ni_{50}Mn_{33.5}In_{16.5})_{98}Ti_2$] (Sánchez-Alarcos et al., 2015). For their studied $(Ni_{50}Mn_{33.5}In_{16.5})_{100-x}Ti_x$ (x = 0, 0.5, 1, and 2) alloys, they found that the Vickers hardness and yield strength increase with the increasing Ti concentration, with an increase of around 10% for $(Ni_{50}Mn_{33.5}In_{16.5})_{98}Ti_2$ compared with the undoped alloy. Q. Shen et al. reported that the Tb doping can reduce the grain size from 50 μm ($Ni_{50}Mn_{34}In_{15.7}Tb_{0.3}$) to 5 μm ($Ni_{50}Mn_{34}In_{15.6}Tb_{0.4}$) (Shen et al., 2017). The compressive strength of $Ni_{50}Mn_{34}In_{15.6}Tb_{0.4}$ increases to 622 MPa from 372 MPa ($Ni_{50}Mn_{34}In_{15.7}Tb_{0.3}$).

b) Grain boundary strengthening: As discussed above, for the NiMnIn compounds, the nucleation and the propagation of

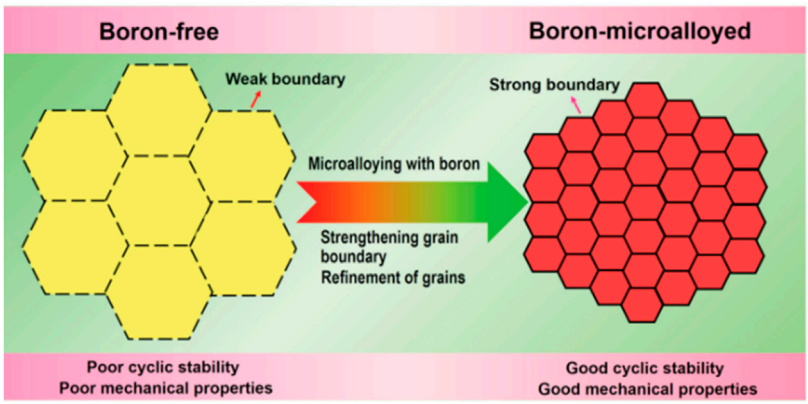

FIGURE 15 | Effects of the B microalloying on the microstructure of a NiMnIn alloy (Yang et al., 2019).

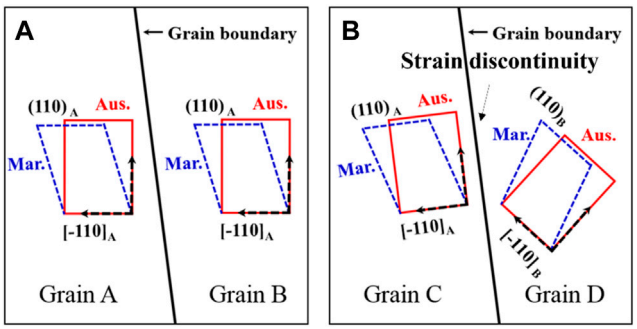

FIGURE 16 | Texture effect on the compatibility of transformation strain around grain boundary. **(A)** strong texture and **(B)** random texture (Huang et al., 2019). Reproduced with the permission of Elsevier Publisher.

cracks mostly occur near grain boundaries of austenite. Thus, elevating the strength of grain boundaries could significantly improve the mechanical properties. Until now, the most effective method known for increasing the cohesion of grain boundary is microalloying with boron (Yang et al., 2017; Yang et al., 2019). Z. Yang et al. reported that by microalloying with boron, as illustrated in **Figure 15**, the grain boundary cohesion can be increased; meanwhile, the grain size can be refined (Yang et al., 2017). With this microstructure modification, the mechanical properties and the eCE cyclic stability of the NiMnIn alloy can be prominently improved. For instance, the eCE of 2 K remains stable with almost no degradation for more than 150 cycles in $(Ni_{51.5}Mn_{33}In_{15.5})_{99.7}B_{0.3}$ (Yang et al., 2017). Later, they realized an ultrahigh cyclability of eCE in the $(Ni_{51}Mn_{33}In_{14}Fe_2)_{99.4}B_{0.6}$ polycrystalline alloy, i.e., a ΔT_{ad} of 5.6 K at 2700 loading-unloading cycles (Yang et al., 2019). With the 3D atom probe tomography (ATP) technique, they reported that the addition of B promotes the formation of NiBH cluster, which may act as the H trapping to reduce the hydrogen diffusion along the grain boundary and thus suppresses the hydrogen embrittlement, leading to an improvement of the grain boundary strength. X. M. Huang et al. found that with the addition of B, the compressive strength σ_{comp} and strain ε_{comp} was significantly improved from 630 MPa to 9.3% of $Ni_{50}Mn_{34.5}In_{15.5}$ alloy to 1142 MPa and 12.3% of $Ni_{50}(Mn_{31.7}Cu_{2.5}B_{0.3})In_{15.5}$ alloy (Huang et al., 2020).

c) Introducing crystallographic texture: The crack nucleation in the NiMnIn alloys is closely related to the discontinuity of transformation strain near the grain boundary regions of austenite with different orientations. Thus, introducing crystallographic texture could effectively reduce the discontinuity of transformation strain at grain boundaries, as illustrated in **Figure 16** (Huang et al., 2019), and thus improve the fracture resistance and the eCE cyclic stability of the NiMnIn alloys. Unlike the conventional metals (such as Al, Cu and Ti) for which the texture can be introduced by severe plastic deformation and heat treatment (Kocks et al., 1998; Yan et al., 2014), the texture of brittle intermetallics can just be introduced at the solidification process, such as the directional solidification and the melt-spinning techniques. Considering the convenience of mechanical loading, the directional solidification technique was widely used to introduce texture for the studies of eCE of the NiMnIn alloys (Huang et al., 2015; Huang et al., 2020).

X. M. Huang et al. systematically studied the influence of microstructural characters on mechanical properties and cyclic stability of eCE using $Ni_{50}Mn_{34.8}In_{15.2}$ as an example material (Huang et al., 2019). By applying arc-melting, suction casting, and directional solidification techniques, three samples with different microstructural features, i.e., arc-melted (columnar-shape grains with the long axis of 1–2 mm and the wide axis of 100–500 μm; random texture), suction cast (grain size less than 200 μm; random texture) and directionally solidified (coarse columnar-shaped grains of several mm; strong <001> texture) samples, were fabricated. The compressive strength and strain of the directionally solidified sample were 991 MPa and 11.9%, respectively, which are obviously higher than the arc-melted (451 MPa and 9.4%) and suction cast (341 MPa and 7%)

samples. Moreover, the cyclic stability of the directionally solidified sample (>40) is much higher than the arc melted and the suction cast samples (<10). These results suggest that the microstructure of the directionally solidified sample, i.e., strong texture and coarse grain, is conducive to obtaining excellent mechanical properties. The improved mechanical properties of the directionally solidified sample are attributed to the reduced strain incompatibility near grain boundaries owing to the strong texture.

d) Introducing a soft second phase: Introducing a soft second phase was also reported to be an effective method to increase the mechanical properties of the NiMnIn-based alloys (Yang et al., 2015; Shen et al., 2018). A. Shen et al. reported that the undoped $Ni_{45}Mn_{37}In_{13}Co_5$ sample with no precipitates could only withstand maximum compressive stress and strain of 155 MPa and 3%. Furthermore, the fracture strength and strain of $Ni_{45}Mn_{36}In_{13}Co_5Cr_1$ with a small amount of the second phase precipitates along grain boundaries increased to 407 MPa and 5% (Shen et al., 2018).

7.3 Perspectives

For the eCE refrigerants, one of the key parameters measuring refrigeration efficiency is ΔT_{ad} or ΔS_{iso}. At present, as discussed in **Section 7.1**, most of the work is focused on reducing the negative contribution of ΔS_{mag} to improve ΔT_{ad}. Apart from the magnetism contribution ΔS_{mag}, ΔT_{ad} is also closely related to the contributions of lattice vibration ΔS_{vib} and electron structure ΔS_{elec}, especially ΔS_{vib}. Thus, increasing ΔS_{vib} could significantly improve the total entropy change ΔS_{str} and further eCE ΔT_{ad}. It is now understood that ΔS_{vib} is associated with the volume change of crystal lattice $\Delta V/V_0$ during martensitic transformation. Thus, elevating $\Delta V/V_0$ would be an effective method to increase eCE ΔT_{ad}. Recently, D. Y. Cong et al. confirmed that a large $\Delta V/V_0$ corresponds to a high value of eCE ΔT_{ad} in the *all-d-metal* NiMnTi alloys (Cong et al., 2019). However, the key materials factors affecting $\Delta V/V_0$ are unknown for certain eCE refrigerants. In addition, for the cyclic stability of eCE, apart from mechanical properties, stress hysteresis is also a critical influencing factor. Generally, a large stress hysteresis is harmful to both the refrigeration efficiency and the functional stability of eCE. However, the key materials factors affecting stress hysteresis also remain unclear. High-throughput experimental techniques, high-throughput first-principle calculations, and machine learning algorithms would provide powerful tools to find the key factors determining ΔV/V0 and stress hysteresis and thus improve the performance of the NiMnIn alloys.

8 SUMMARY

In the past 15 years, stimulated by the potential applications in the fields of smart sensors and solid-state refrigeration, the NiMnIn-based metamagnetic shape memory alloys have attracted increasing attention from both communities of materials science and solid-state physics. Scientists from all over the world have conducted systematic research on the NiMnIn alloy covering from the crystal structure, microstructure, martensitic transformation to metamagnetic shape memory, magnetocaloric, and elastocaloric effects.

The austenite of NiMnIn alloy has a highly ordered cubic $L2_1$ structure. The martensite has a non-modulated (NM) tetragonal or a monoclinic modulated (6M) structure based on the chemical composition. 6M martensite possesses a self-accommodated microstructure with six distinct martensite colonies in one austenite grain. In each colony, there exist four twin-related martensite variants. The Pitsch strain path, $\{01\bar{1}\}_A<0\bar{1}1>_A$, is the real strain path that governs the lattice distortion during martensitic transformation. The progress of metamagnetic shape memory effect was summarized from two aspects of NiCoMnIn and other NiMnIn-based alloys. The magnetocaloric effect was reviewed in the focus of increasing isothermal magnetic entropy change, reducing thermal/magnetism hysteresis, and expanding the operating temperature window. For the elastocaloric effect, the main progress was summarized from two aspects of increasing adiabatic temperature change and improving cyclic stability.

Until now, there are still many fundamental scientific issues to be resolved, including 1) the formation mechanism of modulated martensite structure, 2) the key materials factors that determine the modulation type of martensite, 3) the quantitative relationship between the modulated martensite and functional properties, 4) the reason for the huge difference in detwining stress for different twinning systems, 5) the underlying physical mechanism that the K-S and the Pitsch orientation relations are almost simultaneously satisfied and 6) the shuffling path of the $(001)_M$ atomic layer during the martensitic transformation. To realize practical applications of the fruitful magnetoresponsive and elastocaloric effects, more effective methods to 1) reduce the critical driving field of magnetic-field induced inverse martensitic transformation, 2) decrease the transitional thermal/magnetic/stress hysteresis, and 3) improve mechanical properties and cyclic stability are still in great need.

In recent years, the rapid development of advanced computational characterization methods such as high-throughput first-principles calculations based on quantum mechanics, spherical aberration-corrected TEM electron microscopes, *in-situ* high-resolution TEM electron microscopes, high-throughput experimental methods, and machine learning methods based on big data analyses provide powerful tools for solving the issues mentioned above. The resolution of these issues will definitely promote the development of the NiMn-based magnetic shape memory alloys and the numerous related practical applications.

AUTHOR CONTRIBUTIONS

H-LY and CE conceived and designed the structure of the review. H-LY and X-MH wrote the manuscript. All authors contributed to the discussion and commented on the manuscript.

ACKNOWLEDGMENTS

We would like to thank Dr. Habil. Yudong Zhang for her critical reading and helpful suggestions. The author also thankfully acknowledges the National Natural Science Foundation of China (Grant No. 51801020), the Fundamental Research Funds for the Central Universities (Grant No. N2002005, N2002021), the 111 Project of China (Grant No. BP0719037, B20029), Analytical and Testing Center, Northeastern University, China, LEM3 laboratory, UMR CNRS 7239, Metz, Université de Lorraine, France, and the Heinz Maier-Leibnitz Zentrum, Garching, Germany.

REFERENCES

Abematsu, K., Umetsu, R. Y., Kainuma, R., Kanomata, T., Watanabe, K., and Koyama, K. (2014). Structural and Magnetic Properties of Magnetic Shape Memory Alloy $Ni_{46}Mn_{41}In_{13}$ under Magnetic Fields. *Mater. Trans.* 55, 477–481. doi:10.2320/matertrans.M2013372

Acet, M., Mañosa, L., and Planes, A. (2011). Magnetic-Field-Induced Effects in Martensitic Heusler-Based Magnetic Shape Memory Alloys. *Handbook Magn. Mater.* 19, 231–289. doi:10.1016/b978-0-444-53780-5.00004-1

Bachaga, T., Zhang, J., Khitouni, M., and Sunol, J. J. (2019). NiMn-based Heusler Magnetic Shape Memory Alloys: a Review. *Int. J. Adv. Manuf. Technol.* 103, 2761–2772. doi:10.1007/s00170-019-03534-3

Bai, J., Liu, D., Gu, J., Jiang, X., Liang, X., Guan, Z., et al. (2021). Excellent Mechanical Properties and Large Magnetocaloric Effect of Spark Plasma Sintered Ni-Mn-In-Co alloy. *J. Mater. Sci. Tech.* 74, 46–51. doi:10.1016/j.jmst.2020.10.011

Bain, E. C., and Dunkirk, N. (1924). The Nature of Martensite. *Trans. AIME* 70, 25–47.

Barua, R., Taheri, P., Chen, Y., Koblischka-Veneva, A., Koblischka, M., Jiang, L., et al. (2018). Giant Enhancement of Magnetostrictive Response in Directionally-Solidified $Fe_{83}Ga_{17}Er_x$ Compounds. *Materials* 11, 1039. doi:10.3390/ma11061039

Bechtold, C., Chluba, C., Lima de Miranda, R., and Quandt, E. (2012). High Cyclic Stability of the Elastocaloric Effect in Sputtered TiNiCu Shape Memory Films. *Appl. Phys. Lett.* 101, 091903. doi:10.1063/1.4748307

Brown, G. V. (1976). Magnetic Heat Pumping Near Room Temperature. *J. Appl. Phys.* 47, 3673–3680. doi:10.1063/1.323176

Brown, L. C. (1981). The Thermal Effect in Pseudoelastic Single Crystals of β-CuZnSn. *Mta* 12, 1491–1494. doi:10.1007/bf02643695

Brown, P. J., Bargawi, A. Y., Crangle, J., Neumann, K.-U., and Ziebeck, K. R. A. (1999). Direct Observation of a Band Jahn-Teller Effect in the Martensitic Phase Transition of Ni_2MnGa. *J. Phys. Condens. Matter* 11, 4715–4722. doi:10.1088/0953-8984/11/24/312

Brown, P. J., Crangle, J., Kanomata, T., Matsumoto, M., Neumann, K.-U., Ouladdiaf, B., et al. (2002). The crystal Structure and Phase Transitions of the Magnetic Shape Memory Compound Ni_2MnGa. *J. Phys. Condens. Matter* 14, 10159–10171. doi:10.1088/0953-8984/14/43/313

Bruno, N. M., Wang, S., Karaman, I., and Chumlyakov, Y. I. (2017). Reversible Martensitic Transformation under Low Magnetic Fields in Magnetic Shape Memory Alloys. *Sci. Rep.* 7, 40434. doi:10.1038/srep40434

Bunshah, R., and Mehl, R. (1953). Rate of Propagation of Martensite. *Trans. Am. Inst. Mining Metallurgical Eng.* 197, 1251–1258.

Camarillo, J.-P., Aguilar-Ortiz, C.-O., Flores-Zúñiga, H., Ríos-Jara, D., Soto-Parra, D.-E., Stern-Taulats, E., et al. (2017). Large and Reversible Elastocaloric Effect Near Room Temperature in a Ga-doped Ni-Mn-In Metamagnetic Shape-Memory alloy. *Funct. Mater. Lett.* 10, 1740007. doi:10.1142/s1793604717400070

Camarillo, J.-P., Stern-Taulats, E., Mañosa, L., Flores-Zúñiga, H., Ríos-Jara, D., and Planes, A. (2016). Expanding the Magnetocaloric Operation Range in Ni-Mn-In Heusler Alloys by Cu-Doping. *J. Phys. D: Appl. Phys.* 49, 125006. doi:10.1088/0022-3727/49/12/125006

Cazorla, C. (2019). Novel Mechanocaloric Materials for Solid-State Cooling Applications. *Appl. Phys. Rev.* 6, 041316. doi:10.1063/1.5113620

Chen, L., Hu, F. X., Wang, J., Bao, L. F., Sun, J. R., Shen, B. G., et al. (2012). Magnetoresistance and Magnetocaloric Properties Involving strong Metamagnetic Behavior in Fe-Doped $Ni_{45}(Co_{1-x}Fe_x)_5Mn_{36.6}In_{13.4}$ Alloys. *Appl. Phys. Lett.* 101, 957. doi:10.1063/1.4732525

Chen, X., Srivastava, V., Dabade, V., and James, R. D. (2013). Study of the Cofactor Conditions: Conditions of Supercompatibility between Phases. *J. Mech. Phys. Sol.* 61, 2566–2587. doi:10.1016/j.jmps.2013.08.004

Cheng, P., Zhou, Z., Chen, J., Li, Z., Yang, B., Xu, K., et al. (2021). Combining Magnetocaloric and Elastocaloric Effects in a $Ni_{45}Co_5Mn_{37}In_{13}$ alloy. *J. Mater. Sci. Tech.* 94, 47–52. doi:10.1016/j.jmst.2021.02.071

Chluba, C., Ge, W., Lima de Miranda, R., Strobel, J., Kienle, L., Quandt, E., et al. (2015). Ultralow-fatigue Shape Memory alloy Films. *Science* 348, 1004–1007. doi:10.1126/science.1261164

Christian, J. W. (2002). *The Theory of Transformations in Metals and Alloys*. London: Pergamon Press.

Cong, D., Xiong, W., Planes, A., Ren, Y., Mañosa, L., Cao, P., et al. (2019). Colossal Elastocaloric Effect in Ferroelastic Ni-Mn-Ti Alloys. *Phys. Rev. Lett.* 122, 255703. doi:10.1103/PhysRevLett.122.255703

Crouïgneau, G., Porcar, L., Courtois, P., Pairis, S., Mossang, E., Eyraud, E., et al. (2015). Annealing Effect on the Magnetic Induced Austenite Transformation in Polycrystalline Freestanding Ni-Co-Mn-In Films Produced by Co-sputtering. *J. Appl. Phys.* 117, 035302. doi:10.1063/1.4906224

Cui, J., Wu, Y., Muehlbauer, J., Hwang, Y., Radermacher, R., Fackler, S., et al. (2012). Demonstration of High Efficiency Elastocaloric Cooling with Large ΔT Using NiTi Wires. *Appl. Phys. Lett.* 101, 073904. doi:10.1063/1.4746257

Della Porta, F. (2019). On the Cofactor Conditions and Further Conditions of Supercompatibility between Phases. *J. Mech. Phys. Sol.* 122, 27–53. doi:10.1016/j.jmps.2018.08.012

Devi, P., Singh, S., Dutta, B., Manna, K., D'Souza, S. W., Ikeda, Y., et al. (2018). Adaptive Modulation in the $Ni_2Mn_{1.4}In_{0.6}$ Magnetic Shape-Memory Heusler alloy. *Phys. Rev. B* 97, 224102. doi:10.1103/PhysRevB.97.224102

Dwevedi, S., and Tiwari, B. (2012). Martensitic Transformations and Magnetocaloric Effect in Sn-Doped NiMnIn Shape Memory alloy. *J. Alloys Comp.* 540, 16–20. doi:10.1016/j.jallcom.2012.06.057

Erkartal, B., Duppel, V., Niemann, R., Schultz, L., Fähler, S., Schürmann, U., et al. (2012). Structure and Composition of Magnetocaloric Ni-Mn-In-Co Thin Films on the Nanoscale-A TEM Study. *Adv. Eng. Mater.* 14, 710–715. doi:10.1002/adem.201200072

Feng, Y., Sui, J. H., Gao, Z. Y., Dong, G. F., and Cai, W. (2009). Microstructure, Phase Transitions and Mechanical Properties of $Ni_{50}Mn_{34}In_{16-y}Co_y$ Alloys. *J. Alloys Comp.* 476, 935–939. doi:10.1016/j.jallcom.2008.09.149

Feng, Y., Sui, J. H., Wang, H. B., and Cai, W. (2012). Reversible Magnetic-Field-Induced Phase Transformation and Magnetocaloric Effect above Room Temperature in a Ni-Mn-In-Fe Polycrystal. *J. Magnetism Magn. Mater.* 324, 1982–1984. doi:10.1016/j.jmmm.2012.01.041

Giauque, W. F., and Macdougall, D. P. (1933). Attainment of Temperatures below 1° Absolute by Demagnetization of $Gd_2(SO_4)_3{\cdot}8H_2O$. *Phys. Rev.* 43, 768. doi:10.1103/physrev.43.768

Goetzler, W., Zogg, R., Young, J., and Johnson, C. (2014). *Energy Savings Potential and RD&D Opportunities for Non-vapor-compression HVAC Technologies*. USA: US Department of Energy, Office of Energy Efficiency and Renewable Energy, Building Technologies Office.

Gong, Y.-Y., Wang, D.-H., Cao, Q.-Q., Liu, E.-K., Liu, J., and Du, Y.-W. (2015). Electric Field Control of the Magnetocaloric Effect. *Adv. Mater.* 27, 801–805. doi:10.1002/adma.201404725

Gottschall, T., Gràcia-Condal, A., Fries, M., Taubel, A., Pfeuffer, L., Mañosa, L., et al. (2018). A Multicaloric Cooling Cycle that Exploits thermal Hysteresis. *Nat. Mater* 17, 929–934. doi:10.1038/s41563-018-0166-6

Gottschall, T., Skokov, K. P., Fries, M., Taubel, A., Radulov, I., Scheibel, F., et al. (2019). Making a Cool Choice: The Materials Library of Magnetic Refrigeration. *Adv. Energ. Mater.* 9, 1901322. doi:10.1002/aenm.201901322

Gottschall, T., Skokov, K. P., Frincu, B., and Gutfleisch, O. (2015). Large Reversible Magnetocaloric Effect in Ni-Mn-In-Co. *Appl. Phys. Lett.* 106, 021901. doi:10.1063/1.4905371

Gràcia-Condal, A., Gottschall, T., Pfeuffer, L., Gutfleisch, O., Planes, A., and Mañosa, L. (2020). Multicaloric Effects in Metamagnetic Heusler Ni-Mn-In under Uniaxial Stress and Magnetic Field. *Appl. Phys. Rev.* 7, 041406. doi:10.1063/5.0020755

Guillou, F., Courtois, P., Porcar, L., Plaindoux, P., Bourgault, D., and Hardy, V. (2012). Calorimetric Investigation of the Magnetocaloric Effect in $Ni_{45}Co_5Mn_{37.5}In_{12.5}$. *J. Phys. D: Appl. Phys.* 45, 255001. doi:10.1088/0022-3727/45/25/255001

Han, Z. D., Wang, D. H., Zhang, C. L., Tang, S. L., Gu, B. X., and Du, Y. W. (2006). Large Magnetic Entropy Changes in the $Ni_{45.4}Mn_{41.5}In_{13.1}$ Ferromagnetic Shape Memory alloy. *Appl. Phys. Lett.* 89, 182507. doi:10.1063/1.2385147

Han, Z. D., Wang, D. H., Zhang, C. L., Xuan, H. C., Zhang, J. R., Gu, B. X., et al. (2008). The Phase Transitions, Magnetocaloric Effect, and Magnetoresistance in Co Doped Ni-Mn-Sb Ferromagnetic Shape Memory Alloys. *J. Appl. Phys.* 104, 053906. doi:10.1063/1.2975146

Harris, V. G., and Chen, Y. (2015). Equilibrium Chemical Disorder at the Surface of a Single-Crystal $C1_b$ NiMnSb Half-Heusler Alloy: Implications for Spintronics. *IEEE Magn. Lett.* 6, 1–4. doi:10.1109/lmag.2015.2476778

Hashimoto, T., Kuzuhara, T., Matsumoto, K., Sahashi, M., Inomata, K., Tomokiyo, A., et al. (1987). Investigation of the Magnetic Refrigerant for the Ericsson Magnetic Refrigerator. *Jpn. J. Appl. Phys.* 26, 1673. doi:10.7567/jjaps.26s3.1673

Henández-Navarro, F., Camarillo-Garcia, J. P., Aguilar-Ortiz, C. O., Flores-Zúñiga, H., Ríos, D., González, J. G., et al. (2018). The Influence of Texture on the Reversible Elastocaloric Effect of a Polycrystalline $Ni_{50}Mn_{32}In_{16}Cr_2$ alloy. *Appl. Phys. Lett.* 112, 164101.

Heusler, O. (1934). Kristallstruktur und Ferromagnetismus der Mangan-Aluminium-Kupferlegierungen. *Ann. Phys.* 411, 155–201. doi:10.1002/andp.19344110205

Hu, F.-X., Shen, B.-G., and Sun, J.-R. (2013). Magnetic Entropy Change Involving Martensitic Transition in NiMn-Based Heusler Alloys. *Chin. Phys. B* 22, 037505. doi:10.1088/1674-1056/22/3/037505

Hu, Y., Li, Z., Yang, B., Qian, S., Gan, W., Gong, Y., et al. (2017). Combined Caloric Effects in a Multiferroic Ni-Mn-Ga alloy with Broad Refrigeration Temperature Region. *APL Mater.* 5, 046103. doi:10.1063/1.4980161

Huang, L., Cong, D. Y., Ma, L., Nie, Z. H., Wang, Z. L., Suo, H. L., et al. (2016). Large Reversible Magnetocaloric Effect in a Ni-Co-Mn-In Magnetic Shape Memory alloy. *Appl. Phys. Lett.* 108, 032405. doi:10.1063/1.4940441

Huang, X.-M., Wang, L.-D., Liu, H.-X., Yan, H.-L., Jia, N., Yang, B., et al. (2019). Correlation between Microstructure and Martensitic Transformation, Mechanical Properties and Elastocaloric Effect in Ni-Mn-Based Alloys. *Intermetallics* 113, 106579. doi:10.1016/j.intermet.2019.106579

Huang, X.-M., Zhao, Y., Yan, H.-L., Jia, N., Tang, S., Bai, J., et al. (2020). A Multielement Alloying Strategy to Improve Elastocaloric and Mechanical Properties in Ni-Mn-Based Alloys via Copper and boron. *Scripta Materialia* 185, 94–99. doi:10.1016/j.scriptamat.2020.04.001

Huang, X.-M., Zhao, Y., Yan, H.-L., Jia, N., Yang, B., Li, Z., et al. (2021). Giant Magnetoresistance, Magnetostrain and Magnetocaloric Effects in a Cu-Doped-Textured $Ni_{45}Co_5Mn_{36}In_{13.2}Cu_{0.8}$ Polycrystalline alloy. *J. Alloys Comp.* 889, 161652. doi:10.1016/j.jallcom.2021.161652

Huang, Y. J., Hu, Q. D., Bruno, N. M., Chen, J.-H., Karaman, I., Ross, J. H., et al. (2015). Giant Elastocaloric Effect in Directionally Solidified Ni-Mn-In Magnetic Shape Memory alloy. *Scripta Materialia* 105, 42–45. doi:10.1016/j.scriptamat.2015.04.024

Ito, W., Imano, Y., Kainuma, R., Sutou, Y., Oikawa, K., and Ishida, K. (2007). Martensitic and Magnetic Transformation Behaviors in Heusler-type NiMnIn and NiCoMnIn Metamagnetic Shape Memory Alloys. *Metall. Mat Trans. A.* 38, 759–766. doi:10.1007/s11661-007-9094-9

Ito, W., Nagasako, M., Umetsu, R. Y., Kainuma, R., Kanomata, T., and Ishida, K. (2008). Atomic Ordering and Magnetic Properties in the $Ni_{45}Co_5Mn_{36.7}In_{13.3}$ Metamagnetic Shape Memory alloy. *Appl. Phys. Lett.* 93, 232503. doi:10.1063/1.3043456

Jiang, L., Yang, J., Hao, H., Zhang, G., Wu, S., Chen, Y., et al. (2013). Giant Enhancement in the Magnetostrictive Effect of FeGa Alloys Doped with Low Levels of Terbium. *Appl. Phys. Lett.* 102, 222409. doi:10.1063/1.4809829

Kabirifar, P., Žerovnik, A., Ahčin, Ž., Porenta, L., Brojan, M., and Tušek, J. (2019). Elastocaloric Cooling: State-Of-The-Art and Future Challenges in Designing Regenerative Elastocaloric Devices. *SV-JME* 65, 615–630. doi:10.5545/sv-jme.2019.6369

Kainuma, R., Imano, Y., Ito, W., Sutou, Y., Morito, H., Okamoto, S., et al. (2006). Magnetic-field-induced Shape Recovery by Reverse Phase Transformation. *Nature* 439, 957–960. doi:10.1038/nature04493

Kainuma, R., Oikawa, K., Ito, W., Sutou, Y., Kanomata, T., and Ishida, K. (2008). Metamagnetic Shape Memory Effect in NiMn-Based Heusler-type Alloys. *J. Mater. Chem.* 18, 1837. doi:10.1039/b713947k

Karaca, H. E., Karaman, I., Basaran, B., Lagoudas, D. C., Chumlyakov, Y. I., and Maier, H. J. (2007). On the Stress-Assisted Magnetic-Field-Induced Phase Transformation in Ni_2MnGa Ferromagnetic Shape Memory Alloys. *Acta Materialia* 55, 4253–4269. doi:10.1016/j.actamat.2007.03.025

Karaca, H. E., Karaman, I., Basaran, B., Ren, Y., Chumlyakov, Y. I., and Maier, H. J. (2009). Magnetic Field-Induced Phase Transformation in NiMnCoIn Magnetic Shape-Memory Alloys-A New Actuation Mechanism with Large Work Output. *Adv. Funct. Mater.* 19, 983–998. doi:10.1002/adfm.200801322

Karaca, H., Karaman, I., Basaran, B., Chumlyakov, Y., and Maier, H. (2006). Magnetic Field and Stress Induced Martensite Reorientation in NiMnGa Ferromagnetic Shape Memory alloy Single Crystals. *Acta Materialia* 54, 233–245. doi:10.1016/j.actamat.2005.09.004

Kihara, T., Xu, X., Ito, W., Kainuma, R., and Tokunaga, M. (2014). Direct Measurements of Inverse Magnetocaloric Effects in Metamagnetic Shape-Memory alloy NiCoMnIn. *Phys. Rev. B* 90, 214409. doi:10.1103/PhysRevB.90.214409

Kitanovski, A., and Egolf, P. W. (2009). Application of Magnetic Refrigeration and its Assessment. *J. Magnetism Magn. Mater.* 321, 777–781. doi:10.1016/j.jmmm.2008.11.078

Kocks, U. F., Tome, C. N., Wenk, H. R., and Mecking, H. (1998). *Texture and Anisotropy: Preferred Orientations in Polycrystals and Their Effect on Materials Properties*. Cambridge University Press.

Krenke, T., Acet, M., Wassermann, E. F., Moya, X., Mañosa, L., and Planes, A. (2006). Ferromagnetism in the Austenitic and Martensitic States ofNi–Mn–Inalloys. *Phys. Rev. B* 73. doi:10.1103/PhysRevB.73.174413

Krenke, T., Duman, E., Acet, M., Wassermann, E. F., Moya, X., Mañosa, L., et al. (2007). Magnetic Superelasticity and Inverse Magnetocaloric Effect in Ni-Mn-In. *Phys. Rev. B* 75, 4414. doi:10.1103/physrevb.75.104414

Krenke, T., Duman, E., Acet, M., Wassermann, E. F., Moya, X., Mañosa, L., et al. (2005). Inverse Magnetocaloric Effect in Ferromagnetic Ni-Mn-Sn Alloys. *Nat. Mater* 4, 450–454. doi:10.1038/nmat1395

Kurfiß, M., and Schultz, F. (1930). *Over the Mechanisms of Steel Hardening*, 290–291.

Kurfiß, M., Schultz, F., Anton, R., Meier, G., von Sawilski, L., and Kötzler, J. (2005). Structural and Magnetic Properties of Ni_2MnIn Heusler alloy Films. *J. Magnetism Magn. Mater.* 290, 591–594. doi:10.1016/j.jmmm.2004.11.272

Kustov, S., Corró, M. L., Pons, J., and Cesari, E. (2009). Entropy Change and Effect of Magnetic Field on Martensitic Transformation in a Metamagnetic Ni-Co-Mn-In Shape Memory alloy. *Appl. Phys. Lett.* 94, 191901. doi:10.1063/1.3130229

Li, L., and Yan, M. (2020). Recent Progresses in Exploring the Rare Earth Based Intermetallic Compounds for Cryogenic Magnetic Refrigeration. *J. Alloys Comp.* 823, 153810. doi:10.1016/j.jallcom.2020.153810

Li, Z. B., Zhang, Y. D., Esling, C., Zhao, X., and Zuo, L. (2011a). Determination of the Orientation Relationship between Austenite and Incommensurate 7M Modulated Martensite in Ni-Mn-Ga Alloys. *Acta Materialia* 59, 2762–2772. doi:10.1016/j.actamat.2011.01.015

Li, Z., Dong, S., Li, Z., Yang, B., Liu, F., Sánchez-Valdés, C. F., et al. (2019a). Giant Low-Field Magnetocaloric Effect in Si Alloyed Ni-Co-Mn-In Alloys. *Scripta Materialia* 159, 113–118. doi:10.1016/j.scriptamat.2018.09.029

Li, Z., Jing, C., Zhang, H. L., Yu, D. H., Chen, L., Kang, B. J., et al. (2010). A Large and Reproducible Metamagnetic Shape Memory Effect in Polycrystalline $Ni_{45}Co_5Mn_{37}In_{13}$ Heusler alloy. *J. Appl. Phys.* 108, 113908. doi:10.1063/1.3516487

Li, Z., Li, Z., Li, D., Yang, J., Yang, B., Hu, Y., et al. (2020). Achieving a Broad Refrigeration Temperature Region through the Combination of Successive Caloric Effects in a Multiferroic $Ni_{50}Mn_{35}In_{15}$ alloy. *Acta Materialia* 192, 52–59. doi:10.1016/j.actamat.2020.03.043

Li, Z., Li, Z., Li, D., Yang, J., Yang, B., Wang, D., et al. (2019c). Influence of Austenite Ferromagnetism on the Elastocaloric Effect in a $Ni_{44.9}Co_{4.9}Mn_{36.9}In_{13.3}$ Metamagnetic Shape Memory alloy. *Appl. Phys. Lett.* 115, 083903. doi:10.1063/1.5114997

Li, Z., Li, Z., Yang, B., Zhao, X., and Zuo, L. (2018). Giant Low-Field Magnetocaloric Effect in a Textured $Ni_{45.3}Co_{5.1}Mn_{36.1}In_{13.5}$ alloy. *Scripta Materialia* 151, 61–65. doi:10.1016/j.scriptamat.2018.03.043

Li, Z., Xu, K., Yang, H. M., Zhang, Y. L., and Jing, C. (2015). Magnetostrain and Magnetocaloric Effect by Field-Induced Reverse Martensitic Transformation for Pd-Doped $Ni_{45}Co_5Mn_{37}In_{13}$ Heusler alloy. *J. Appl. Phys.* 117, 223904. doi:10.1063/1.4922579

Li, Z., Yang, J., Li, D., Li, Z., Yang, B., Yan, H., et al. (2019b). Tuning the Reversible Magnetocaloric Effect in Ni-Mn-In-Based Alloys through Co and Cu Co-Doping. *Adv. Electron. Mater.* 5, 1800845. doi:10.1002/aelm.201800845

Li, Z., Zhang, Y., Esling, C., Zhao, X., and Zuo, L. (2011b). Determination of the Orientation Relationship between Austenite and 5M Modulated Martensite in Ni-Mn-Ga Alloys. *J. Appl. Cryst.* 44, 1222–1226. doi:10.1107/S0021889811043366

Liang, X., Bai, J., Guan, Z., Gu, J., Yan, H., Zhang, Y., et al. (2021). Revealing the Role of Site Occupation in Phase Stability, Magnetic and Electronic Properties of Ni-Mn-In Alloys by Ab Initio Approach. *J. Mater. Sci. Tech.* 83, 90–101. doi:10.1016/j.jmst.2020.12.040

Lin, C., Yan, H., Zhang, Y., Esling, C., Zhao, X., and Zuo, L. (2016). Crystal Structure of Modulated Martensite and Crystallographic Correlations between Martensite Variants of $Ni_{50}Mn_{38}Sn_{12}$ alloy. *J. Appl. Cryst.* 49, 1276–1283. doi:10.1107/S1600576716010372

Lin, J., Tong, P., Zhang, X., Wang, Z., Zhang, Z., Li, B., et al. (2020). Giant Room-Temperature Barocaloric Effect at the Electronic Phase Transition in $Ni_{1-x}Fe_xS$. *Mater. Horiz.* 7, 2690–2695. doi:10.1039/C9MH01976F

Liu, G. D., Dai, X. F., Yu, S. Y., Zhu, Z. Y., Chen, J. L., Wu, G. H., et al. (2006). Physical and Electronic Structure and Magnetism of Mn_2NiGa: Experiment and Density-Functional Theory Calculations. *Phys. Rev. B* 74. doi:10.1103/physrevb.74.054435

Liu, J., Aksoy, S., Scheerbaum, N., Acet, M., and Gutfleisch, O. (2009a). Large Magnetostrain in Polycrystalline Ni–Mn–In–Co. *Appl. Phys. Lett.* 95, 1746. doi:10.1063/1.3249585

Liu, J., Gottschall, T., Skokov, K. P., Moore, J. D., and Gutfleisch, O. (2012). Giant Magnetocaloric Effect Driven by Structural Transitions. *Nat. Mater* 11, 620–626. doi:10.1038/nmat3334

Liu, J., Scheerbaum, N., Hinz, D., and Gutfleisch, O. (2008). Magnetostructural Transformation in Ni-Mn-In-Co Ribbons. *Appl. Phys. Lett.* 92, 162509. doi:10.1063/1.2913162

Liu, J., Woodcock, T. G., Scheerbaum, N., and Gutfleisch, O. (2009b). Influence of Annealing on Magnetic Field-Induced Structural Transformation and Magnetocaloric Effect in Ni-Mn-In-Co Ribbons. *Acta Materialia* 57, 4911–4920. doi:10.1016/j.actamat.2009.06.054

Liu, J., Zhao, D., and Li, Y. (2017). Exploring Magnetic Elastocaloric Materials for Solid-State Cooling. *Shap. Mem. Superelasticity* 3, 192–198. doi:10.1007/s40830-017-0118-z

Liu, X., Raulot, J.-M., Esling, C., Zhao, X., and Zuo, L. (2020). Investigation on the Preference of the Martensitic Structure in Off-Stoichiometric Ni-Mn-In Alloys by First-Principle Calculations. *J. Magnetism Magn. Mater.* 514, 167194. doi:10.1016/j.jmmm.2020.167194

Liu, Z. H., Aksoy, S., and Acet, M. (2009c). Influence of Sb on the Magnetic and Magnetocaloric Properties of Ferromagnetic Shape Memory alloy NiMnIn. *J. Appl. Phys.* 105, 033913. doi:10.1063/1.3075821

Lu, B., and Liu, J. (2017). Elastocaloric Effect and Superelastic Stability in Ni-Mn-In-Co Polycrystalline Heusler Alloys: Hysteresis and Strain-Rate Effects. *Sci. Rep.* 7, 1–11. doi:10.1038/s41598-017-02300-3

Lu, B., Xiao, F., Yan, A., and Liu, J. (2014). Elastocaloric Effect in a Textured Polycrystalline Ni-Mn-In-Co Metamagnetic Shape Memory alloy. *Appl. Phys. Lett.* 105, 161905. doi:10.1063/1.4899147

Lu, B., Zhang, P., Xu, Y., Sun, W., and Liu, J. (2015). Elastocaloric Effect in $Ni_{45}Mn_{36.4}In_{13.6}Co_5$ Metamagnetic Shape Memory Alloys under Mechanical Cycling. *Mater. Lett.* 148, 110–113. doi:10.1016/j.matlet.2015.02.076

Luo, Q., and Wang, W. H. (2009). Rare Earth Based Bulk Metallic Glasses. *J. Non-Crystalline Sol.* 355, 759–775. doi:10.1016/j.jnoncrysol.2009.02.006

Mañosa, L., González-Alonso, D., Planes, A., Bonnot, E., Barrio, M., Tamarit, J.-L., et al. (2010). Giant Solid-State Barocaloric Effect in the Ni-Mn-In Magnetic Shape-Memory alloy. *Nat. Mater* 9, 478–481. doi:10.1038/nmat2731

Mañosa, L., Gonzalez-Comas, A., Obradó, E., Planes, A., Chernenko, V., Kokorin, V., et al. (1997). Anomalies Related to the TA_2-Phonon-Mode Condensation in the Heusler Ni_2MnGa alloy. *Phys. Rev. B* 55, 11068.

Mañosa, L., and Planes, A. (2017). Materials with Giant Mechanocaloric Effects: Cooling by Strength. *Adv. Mater.* 29, 1603607. doi:10.1002/adma.201603607

McMichael, R. D., Ritter, J. J., and Shull, R. D. (1993). Enhanced Magnetocaloric Effect in $Gd_3Ga_{5-x}Fe_xO_{12}$. *J. Appl. Phys.* 73, 6946–6948. doi:10.1063/1.352443

Monroe, J. A., Karaman, I., Basaran, B., Ito, W., Umetsu, R. Y., Kainuma, R., et al. (2012). Direct Measurement of Large Reversible Magnetic-Field-Induced Strain in Ni-Co-Mn-In Metamagnetic Shape Memory Alloys. *Acta Materialia* 60, 6883–6891. doi:10.1016/j.actamat.2012.07.040

Moya, X., Kar-Narayan, S., and Mathur, N. D. (2014). Caloric Materials Near Ferroic Phase Transitions. *Nat. Mater* 13, 439–450. doi:10.1038/nmat3951

Mukherjee, K. (1968). On the Dynamics of Martensitic Transformation. *Trans. Met. Soc. AIME* 242, 1494–1501.

Murray, S. J., Marioni, M., Allen, S. M., O'Handley, R. C., and Lograsso, T. A. (2000). 6% Magnetic-Field-Induced Strain by Twin-Boundary Motion in Ferromagnetic Ni–Mn–Ga. *Appl. Phys. Lett.* 77, 886–888.

Nikitin, S. A. (2011). Magnetoelastic and Elastocaloric Effects in Rare-Earth Metals, Their Alloys and Compounds in the Region of Magnetic Phase Transitions, *Mosc. Univ. Phys.*, 66. 519–533. Their Alloys and Compounds in the Region of Magnetic Phase Transitions. doi:10.3103/s0027134911060130

Nirmala, R., Morozkin, A. V., and Malik, S. K. (2015). Magnetocaloric Effect in Rare-Earth Intermetallics: Recent Trends. *Pramana - J. Phys.* 84, 977–985. doi:10.1007/s12043-015-1000-1

Nishiyama, Z. (1978). *Martensitic Transformation*. New York: Academic Press.

Nishiyama, Z. (1934). X-ray Investigation of the Mechanism of the Transformation from Face Centered Cubic Lattice to Body Centered Cubic. *Sci. Rep. Tohoku Univ.* 23, 637.

Paramanik, T., and Das, I. (2016). Near Room Temperature Giant Magnetocaloric Effect and Giant Negative Magnetoresistance in Co, Ga Substituted Ni-Mn-In Heusler alloy. *J. Alloys Comp.* 654, 399–403. doi:10.1016/j.jallcom.2015.09.096

Pataky, G. J., Ertekin, E., and Sehitoglu, H. (2015). Elastocaloric Cooling Potential of NiTi, Ni_2FeGa, and CoNiAl. *Acta Materialia* 96, 420–427. doi:10.1016/j.actamat.2015.06.011

Pathak, A. K., Dubenko, I., Pueblo, C., Stadler, S., and Ali, N. (2010). Magnetism and Magnetocaloric Effects in $Ni_{50}Mn_{35-x}Co_xIn_{15}$ Heusler Alloys. *J. Appl. Phys.* 107, 09A907. doi:10.1063/1.3335893

Pecharsky, V. K., and Gschneidner, Jr., K. A., Jr. (1997). Giant Magnetocaloric Effect in $Gd_5(Si_2Ge_2)$. *Phys. Rev. Lett.* 78, 4494–4497. doi:10.1103/PhysRevLett.78.4494

Pitsch, W. (1962). Der orientierungszusammenhang zwischen zementit und austenit. *Acta Metallurgica* 10, 897–900. doi:10.1016/0001-6160(62)90108-6

Planes, A., Obradó, E., Gonzàlez-Comas, A., and Mañosa, L. (1997). Premartensitic Transition Driven by Magnetoelastic Interaction in Bcc Ferromagnetic Ni_2MnGa. *Phys. Rev. Lett.* 79, 3926–3929. doi:10.1103/PhysRevLett.79.3926

Pons, J., Chernenko, V. A., Santamarta, R., and Cesari, E. (2000). Crystal Structure of Martensitic Phases in Ni-Mn-Ga Shape Memory Alloys. *Acta Materialia* 48, 3027–3038. doi:10.1016/s1359-6454(00)00130-0

Qian, S., Ling, J., Hwang, Y., Radermacher, R., and Takeuchi, I. (2015). Thermodynamics Cycle Analysis and Numerical Modeling of Thermoelastic Cooling Systems. *Int. J. Refrigeration* 56, 65–80. doi:10.1016/j.ijrefrig.2015.04.001

Raphael, M. P., Ravel, B., Huang, Q., Willard, M. A., Cheng, S. F., Das, B. N., et al. (2002). Presence of Antisite Disorder and its Characterization in the Predicted Half-metal Co_2MnSi. *Phys. Rev. B* 66, 104429. doi:10.1103/physrevb.66.104429

Ravel, B., Cross, J. O., Raphael, M. P., Harris, V. G., Ramesh, R., and Saraf, L. V. (2002a). Atomic Disorder in Heusler Co_2MnGe Measured by Anomalous X-ray Diffraction. *Appl. Phys. Lett.* 81, 2812–2814. doi:10.1063/1.1513216

Ravel, B., Raphael, M. P., Harris, V. G., and Huang, Q. (2002b). EXAFS and Neutron Diffraction Study of the Heusler alloy Co_2MnSi. *Phys. Rev. B* 65, 184431. doi:10.1103/physrevb.65.184431

Recarte, V., Pérez-Landazábal, J. I., Gómez-Polo, C., Sánchez-Alarcos, V., Cesari, E., and Pons, J. (2010). Vibrational and Magnetic Contributions to the Entropy Change Associated with the Martensitic Transformation of Ni-Fe-Ga

Ferromagnetic Shape Memory Alloys. *J. Phys. Condens. Matter* 22, 416001. doi:10.1088/0953-8984/22/41/416001

Recarte, V., Pérez-Landazábal, J. I., Sánchez-Alarcos, V., Zablotskii, V., Cesari, E., and Kustov, S. (2012). Entropy Change Linked to the Martensitic Transformation in Metamagnetic Shape Memory Alloys. *Acta Materialia* 60, 3168–3175. doi:10.1016/j.actamat.2012.02.022

Sakon, T., Yamazaki, S., Kodama, Y., Motokawa, M., Kanomata, T., Oikawa, K., et al. (2007). Magnetic Field-Induced Strain of Ni-Co-Mn-In Alloy in Pulsed Magnetic Field. *Jpn. J. Appl. Phys.* 46, 995–998. doi:10.1143/jjap.46.995

Sánchez-Alarcos, V., Pérez-Landazábal, J. I., Recarte, V., and Urdiaín, A. (2015). Effect of Ti Addition on the Mechanical Properties and the Magnetocaloric Effect of Ni-Mn-In Metamagnetic Shape Memory Alloys. *J. Phys. D: Appl. Phys.* 48, 445006. doi:10.1088/0022-3727/48/44/445006

Şaşıoğlu, E., Sandratskii, L. M., and Bruno, P. (2004). First-principles Calculation of the Intersublattice Exchange Interactions and Curie Temperatures of the Full Heusler alloys Ni_2MnX(X=Ga,In,Sn,Sb). *Phys. Rev. B* 70, 024427. doi:10.1103/PhysRevB.70.024427

Schmidt, M., Schütze, A., and Seelecke, S. (2015). Scientific Test Setup for Investigation of Shape Memory alloy Based Elastocaloric Cooling Processes. *Int. J. Refrigeration* 54, 88–97. doi:10.1016/j.ijrefrig.2015.03.001

Sharma, V. K., Chattopadhyay, M. K., Khandelwal, A., and Roy, S. B. (2010a). Martensitic Transition Near Room Temperature and the Temperature- and Magnetic-Field-Induced Multifunctional Properties of $Ni_{49}CuMn_{34}In_{16}$ alloy. *Phys. Rev. B* 82, 172411. doi:10.1103/PhysRevB.82.172411

Sharma, V. K., Chattopadhyay, M. K., and Roy, S. B. (2010b). Large Magnetocaloric Effect in $Ni_{50}Mn_{33.66}Cr_{0.34}In_{16}$ alloy. *J. Phys. D: Appl. Phys.* 43, 225001. doi:10.1088/0022-3727/43/22/225001

Sharma, V. K., Chattopadhyay, M. K., Sharath Chandra, L. S., and Roy, S. B. (2011). Elevating the Temperature Regime of the Large Magnetocaloric Effect in a Ni-Mn-In alloy towards Room Temperature. *J. Phys. D: Appl. Phys.* 44, 145002. doi:10.1088/0022-3727/44/14/145002

Shen, A., Sun, W., Zhao, D., and Liu, J. (2018). Influence of Cr on Microstructure and Elastocaloric Effect in Ni-Mn-In-Co-Cr Polycrystalline Alloys. *Phys. Lett. A* 382, 2876–2879. doi:10.1016/j.physleta.2018.06.022

Shen, Q., Zhao, D., Sun, W., Li, Y., and Liu, J. (2017). The Effect of Tb on Elastocaloric and Mechanical Properties of Ni-Mn-In-Tb Alloys. *J. Alloys Comp.* 696, 538–542. doi:10.1016/j.jallcom.2016.11.290

Song, Y., Chen, X., Dabade, V., Shield, T. W., and James, R. D. (2013). Enhanced Reversibility and Unusual Microstructure of a Phase-Transforming Material. *Nature* 502, 85–88. doi:10.1038/nature12532

Stern-Taulats, E., Castán, T., Mañosa, L., Planes, A., Mathur, N. D., and Moya, X. (2018). Multicaloric Materials and Effects. *MRS Bull.* 43, 295–299. doi:10.1557/mrs.2018.72

Sutou, Y., Imano, Y., Koeda, N., Omori, T., Kainuma, R., Ishida, K., et al. (2004a). Magnetic and Martensitic Transformations of NiMnX(X=In,Sn,Sb) Ferromagnetic Shape Memory Alloys. *Appl. Phys. Lett.* 85, 4358. doi:10.1063/1.1808879

Sutou, Y., Imano, Y., Koeda, N., Omori, T., Kainuma, R., Ishida, K., et al. (2004b). Magnetic and Martensitic Transformations of NiMnX(X=In,Sn,Sb) Ferromagnetic Shape Memory Alloys. *Appl. Phys. Lett.* 85, 4358–4360. doi:10.1063/1.1808879

Tang, X., Feng, Y., Wang, H., and Wang, P. (2019). Enhanced Elastocaloric Effect and Cycle Stability in B and Cu Co-doping Ni-Mn-In Polycrystals. *Appl. Phys. Lett.* 114, 033901. doi:10.1063/1.5080762

Tegus, O., Brück, E., Zhang, L., Dagula, K., Buschow, K. H. J., and de Boer, F. R. (2002). Magnetic-phase Transitions and Magnetocaloric Effects. *Physica B: Condensed Matter* 319, 174–192. doi:10.1016/S0921-4526(02)01119-5

Turabi, A. S., Karaca, H. E., Tobe, H., Basaran, B., Aydogdu, Y., and Chumlyakov, Y. I. (2016). Shape Memory Effect and Superelasticity of NiMnCoIn Metamagnetic Shape Memory Alloys under High Magnetic Field. *Scripta Materialia* 111, 110–113. doi:10.1016/j.scriptamat.2015.08.027

Tušek, J., Engelbrecht, K., Eriksen, D., Dall'Olio, S., Tušek, J., and Pryds, N. (2016). A Regenerative Elastocaloric Heat Pump. *Nat. Energ.* 1. doi:10.1038/nenergy.2016.134

Tušek, J., Engelbrecht, K., Mikkelsen, L. P., and Pryds, N. (2015). Elastocaloric Effect of Ni-Ti Wire for Application in a Cooling Device. *J. Appl. Phys.* 117, 124901. doi:10.1063/1.4913878

Ullakko, K., Huang, J. K., Kantner, C., O'Handley, R. C., and Kokorin, V. V. (1996). Large Magnetic-field-induced Strains in Ni_2MnGa Single Crystals. *Appl. Phys. Lett.* 69, 1966–1968. doi:10.1063/1.117637

Ullakko, K., Huang, J. K., Kokorin, V. V., and O'Handley, R. C. (1997). Magnetically Controlled Shape Memory Effect in Ni_2MnGa Intermetallics. *Scripta Materialia* 36, 1133–1138. doi:10.1016/s1359-6462(96)00483-6

Van Smaalen, S. (1995). Incommensurate crystal Structures. *Crystallogr. Rev.* 4, 79–202. doi:10.1080/08893119508039920

Wang, J., Yu, Q., Xu, K., Zhang, C., Wu, Y., and Jiang, C. (2017). Large Room-Temperature Elastocaloric Effect of $Ni_{57}Mn_{18}Ga_{21}In_4$ alloy Undergoing a Magnetostructural Coupling Transition. *Scripta Materialia* 130, 148–151. doi:10.1016/j.scriptamat.2016.11.024

Wang, L., Li, Z., Yang, J., Yang, B., Zhao, X., and Zuo, L. (2020). Large Refrigeration Capacity in a $Ni_{48}Co_1Mn_{37}In_{14}$ Polycrystalline alloy with Low thermal Hysteresis. *Intermetallics* 125, 106888. doi:10.1016/j.intermet.2020.106888

Wang, Y. D., Ren, Y., Huang, E. W., Nie, Z. H., Wang, G., Liu, Y. D., et al. (2007). Direct Evidence on Magnetic-Field-Induced Phase Transition in a NiCoMnIn Ferromagnetic Shape Memory alloy under a Stress Field. *Appl. Phys. Lett.* 90, 101917. doi:10.1063/1.2712509

Wei, Z. Y., Liu, E. K., Li, Y., Han, X. L., Du, Z. W., Luo, H. Z., et al. (2016). Magnetostructural Martensitic Transformations with Large Volume Changes and Magneto-Strains in All-D-Metal Heusler Alloys. *Appl. Phys. Lett.* 109, 071904. doi:10.1063/1.4961382

Wiedemann, G. (1889). Magnetische Untersuchungen. *Ann. Phys.* 273, 610–628. doi:10.1002/andp.18892730806

Wirth, S., Leithe-Jasper, A., Vasil, A. N. E., and Coey, J. M. D. (1997). Structural and Magnetic Properties of Ni_2MnGa. *J. Magn. Magn. Mater.* 167. doi:10.1016/S0304-8853(96)00745-7

Yan, H.-L., Huang, X.-M., Yang, J.-H., Zhao, Y., Fang, F., Jia, N., et al. (2021a). A Strategy of Optimizing Magnetism and Hysteresis Simultaneously in Ni-Mn-Based Metamagnetic Shape Memory Alloys. *Intermetallics* 130, 107063. doi:10.1016/j.intermet.2020.107063

Yan, H.-L., Liu, H.-X., Huang, X.-M., Zhang, M.-J., Jia, N., Bai, J., et al. (2020a). First-principles Investigation of Mg Substitution for Ga on Martensitic Transformation, Magnetism and Electronic Structures in Ni_2MnGa. *J. Alloys Comp.* 843, 156049. doi:10.1016/j.jallcom.2020.156049

Yan, H.-L., Wang, L.-D., Liu, H.-X., Huang, X.-M., Jia, N., Li, Z.-B., et al. (2019). Giant Elastocaloric Effect and Exceptional Mechanical Properties in an All-D-Metal Ni-Mn-Ti alloy: Experimental and Ab-Initio Studies. *Mater. Des.* 184, 108180. doi:10.1016/j.matdes.2019.108180

Yan, H.-L., Zhang, Y., Esling, C., Zhao, X., and Zuo, L. (2021b). Determination of Strain Path during Martensitic Transformation in Materials with Two Possible Transformation Orientation Relationships from Variant Self-Organization. *Acta Materialia* 202, 112–123. doi:10.1016/j.actamat.2020.10.054

Yan, H.-L., Zhao, Y., Liu, H.-X., Zhang, M.-J., Zhang, H.-F., Bai, J., et al. (2020b). Ab-initio Revelation on the Origins of Ti Substitution for Ga, Mn and Ni on Ferromagnetism, Phase Stability and Elastic Properties in Ni_2MnGa. *J. Alloys Comp.* 821, 153481. doi:10.1016/j.jallcom.2019.153481

Yan, H., Yang, B., Zhang, Y., Li, Z., Esling, C., Zhao, X., et al. (2016a). Variant Organization and Mechanical Detwinning of Modulated Martensite in Ni-Mn-In Metamagnetic Shape-Memory Alloys. *Acta Materialia* 111, 75–84. doi:10.1016/j.actamat.2016.03.049

Yan, H., Yang, B., Zhang, Y., Li, Z., Esling, C., Zhao, X., et al. (2016b). Variant Organization and Mechanical Detwinning of Modulated Martensite in Ni-Mn-In Metamagnetic Shape-Memory Alloys. *Acta Materialia* 111, 75–84. doi:10.1016/j.actamat.2016.03.049

Yan, H., Zhang, C., Zhang, Y., Wang, X., Esling, C., Zhao, X., et al. (2016c). Crystallographic Insights into Ni-Co-Mn-In Metamagnetic Shape Memory Alloys. *J. Appl. Cryst.* 49, 1585–1592. doi:10.1107/s1600576716012140

Yan, H., Zhang, Y., Xu, N., Senyshyn, A., Brokmeier, H.-G., Esling, C., et al. (2015). Crystal Structure Determination of Incommensurate Modulated Martensite in Ni-Mn-In Heusler Alloys. *Acta Materialia* 88, 375–388. doi:10.1016/j.actamat.2015.01.025

Yan, H., Zhao, X., Jia, N., Zheng, Y., and He, T. (2014). Influence of Shear Banding on the Formation of Brass-type Textures in Polycrystalline Fcc Metals with Low Stacking Fault Energy. *J. Mater. Sci. Tech.* 30, 408–416. doi:10.1016/j.jmst.2013.11.010

Yang, S. Y., Liu, Y. D., Wang, C. P., Lu, Y., Wang, J. M., Shi, Z., et al. (2015). Microstructure and Functional Properties of Two-phase Ni-Mn-Fe-In Shape

Memory Alloys with Small Transformation Hysteresis Width. *J. Alloys Comp.* 619, 498–504. doi:10.1016/j.jallcom.2014.09.079

Yang, Y., Li, Z., Sánchez-Valdés, C. F., Sánchez Llamazares, J. L., Yang, B., Zhang, Y., et al. (2020). Phase Transformation and Magnetocaloric Effect of Co-doped Mn-Ni-In Melt-Spun Ribbons. *J. Appl. Phys.* 128, 055110. doi:10.1063/5.0014883

Yang, Z., Cong, D. Y., Huang, L., Nie, Z. H., Sun, X. M., Zhang, Q. H., et al. (2016). Large Elastocaloric Effect in a Ni-Co-Mn-Sn Magnetic Shape Memory alloy. *Mater. Des.* 92, 932–936. doi:10.1016/j.matdes.2015.12.118

Yang, Z., Cong, D. Y., Sun, X. M., Nie, Z. H., and Wang, Y. D. (2017). Enhanced Cyclability of Elastocaloric Effect in boron-microalloyed Ni-Mn-In Magnetic Shape Memory Alloys. *Acta Materialia* 127, 33–42. doi:10.1016/j.actamat.2017.01.025

Yang, Z., Cong, D., Yuan, Y., Wu, Y., Nie, Z., Li, R., et al. (2019). Ultrahigh Cyclability of a Large Elastocaloric Effect in Multiferroic Phase-Transforming Materials. *Mater. Res. Lett.* 7, 137–144. doi:10.1080/21663831.2019.1566182

Yu, B., Liu, M., Egolf, P. W., and Kitanovski, A. (2010). A Review of Magnetic Refrigerator and Heat Pump Prototypes Built before the Year 2010. *Int. J. Refrigeration* 33, 1029–1060. doi:10.1016/j.ijrefrig.2010.04.002

Yu, S. Y., Gu, A. J., Kang, S. S., Hu, S. J., Li, Z. C., Ye, S. T., et al. (2016). Large Reversible Magnetostrain in Polycrystalline $Ni_{50}Mn_{33}In_{17-x}Ga_x$. *J. Alloys Comp.* 681, 1–5. doi:10.1016/j.jallcom.2016.04.249

Yu, S. Y., Wei, J. J., Kang, S. S., Chen, J. L., and Wu, G. H. (2014). Large Temperature and Magnetic Field Induced Strain in Polycrystalline $Ni_{50}Mn_{36}In_{14-x}Sb_x$ Alloys. *J. Alloys Comp.* 586, 328–332. doi:10.1016/j.jallcom.2013.10.072

Zhang, C., Yan, H., Zhang, Y., Esling, C., Zhao, X., and Zuo, L. (2016). Crystal Structure and Crystallographic Characteristics of Martensite in $Ni_{50}Mn_{38}Sb_{12}$ Alloys. *J. Appl. Cryst.* 49, 513–519. doi:10.1107/S1600576716002296

Zhang, J., Xu, Y., An, S., Sun, Y., Li, X., and Li, Y. (2020). Giant Mechanocaloric Materials for Solid-State Cooling*. *Chin. Phys. B* 29, 076202. doi:10.1088/1674-1056/ab8a40

Zhang, X.-x., Miao, S.-p., and Sun, J.-f. (2014). Magnetocaloric Effect in Ni-Mn-In-Co Microwires Prepared by Taylor-Ulitovsky Method. *Trans. Nonferrous Met. Soc. China* 24, 3152–3157. doi:10.1016/s1003-6326(14)63454-3

Zhang, Y. D., Esling, C., Zhao, X., and Zuo, L. (2007). Indirect Two-Trace Method to Determine a Faceted Low-Energy Interface between Two Crystallographically Correlated Crystals. *J. Appl. Cryst.* 40, 436–440. doi:10.1107/s0021889807014331

Zhang, Y., Li, Z., Esling, C., Muller, J., Zhao, X., and Zuo, L. (2010). A General Method to Determine Twinning Elements. *J. Appl. Cryst.* 43, 1426–1430. doi:10.1107/s0021889810037180

Zhao, D., Liu, J., Chen, X., Sun, W., Li, Y., Zhang, M., et al. (2017a). Giant Caloric Effect of Low-Hysteresis Metamagnetic Shape Memory Alloys with Exceptional Cyclic Functionality. *Acta Materialia* 133, 217–223. doi:10.1016/j.actamat.2017.05.020

Zhao, D., Liu, J., Feng, Y., Sun, W., and Yan, A. (2017b). Giant Elastocaloric Effect and its Irreversibility in [001]-oriented $Ni_{45}Mn_{36.5}In_{13.5}Co_5$ Meta-Magnetic Shape Memory Alloys. *Appl. Phys. Lett.* 110, 021906. doi:10.1063/1.4973965

Zheludev, A., Shapiro, S. M., Wochner, P., and Tanner, L. E. (1996). Precursor Effects and Premartensitic Transformation in Ni_2MnGa. *Phys. Rev. B* 54, 15045–15050. doi:10.1103/physrevb.54.15045

Conflict of Interest: The authors declare that the research was conducted in the absence of any commercial or financial relationships that could be construed as a potential conflict of interest.

Publisher's Note: All claims expressed in this article are solely those of the authors and do not necessarily represent those of their affiliated organizations, or those of the publisher, the editors and the reviewers. Any product that may be evaluated in this article, or claim that may be made by its manufacturer, is not guaranteed or endorsed by the publisher.